

## Applicability of InSAR to tropical volcanoes: insights from Central America

S. K. EBMEIER<sup>1,2\*</sup>, J. BIGGS<sup>2,3</sup>, T. A. MATHER<sup>1</sup> & F. AMELUNG<sup>3</sup>

<sup>1</sup>COMET+, Department of Earth Sciences, University of Oxford,  
South Parks Road, Oxford OX1 3AN, UK

<sup>2</sup>COMET+, School of Earth Sciences, University of Bristol, Wills Memorial  
Building, Queens Road, Bristol BS8 1RJ, UK

<sup>3</sup>RSMAS, University of Miami, 4600 Rickenbacker Causeway, Miami, FL 33149, USA

\*Corresponding author (e-mail: [sk.ebmeier@bristol.ac.uk](mailto:sk.ebmeier@bristol.ac.uk))

**Abstract:** Measuring volcano deformation is key to understanding the behaviour of erupting volcanoes and detecting those in periods of unrest. Satellite techniques provide the opportunity to do so on a global scale but, with some notable exceptions, the deformation of volcanoes in the tropics has been understudied relative to those at higher latitudes, largely due to technical difficulties in applying Interferometric Synthetic Aperture Radar (InSAR).

We perform a systematic survey of the Central American Volcanic Arc to investigate the applicability of Interferometric Synthetic Aperture Radar (InSAR) to volcanoes in the tropics. Volcano characteristics that may prevent InSAR measurement include: (1) dense vegetation cover; (2) persistent activity; and (3) steep slopes. Measurements of deformation are further inhibited by atmospheric artefacts associated with: (4) large changes in topographical relief. We present a systematic method for distinguishing between water vapour artefacts and true deformation. Our data show a linear relationship (c. 2 cm/km) between the magnitudes of water vapour artefacts and volcano edifice height. For high relief volcanoes (e.g. Fuego, Guatemala, 3763 m a.s.l. (above sea level)) errors are of the order of 4–5 cm across the volcano's edifice but are less than 2 cm for lower relief (e.g. Masaya, Nicaragua, 635 m a.s.l.). Examples such as Arenal, Atitlan and Fuego illustrate that satellite acquisition strategies incorporating ascending and descending tracks are particularly important for studying steep-sided volcanoes.

Poor coherence is primarily associated with temporal decorrelation, which is typically more rapid in southern Central America where Evergreen broadleaf vegetation dominates. Land-use classification is a better predictor of decorrelation rate than vegetation index. Comparison of coherence for different radar wavelengths match expectations; high resolution X-band radar is best suited to local studies where high-resolution digital elevation models (DEMs) exist, while L-band wavelengths are necessary for regional surveys. However, this is the first time that relationships between phase coherence and time, perpendicular baseline, radar wavelength, and land use have been quantified on the scale of a whole volcanic arc.

Interferometric synthetic aperture radar has been used to detect and measure deformation at over 70 volcanoes worldwide since the 1990s (Fournier *et al.* 2010). A variety of different types of deformation have been observed using InSAR surveys, including the movement of magma during co-eruptive deformation (e.g. Lu & Dzurisin 2010) or intrusive processes (e.g. dyke and sill intrusion: Hamling *et al.* 2009; Biggs *et al.* 2010), as well as a variety of shallower surface processes. These include hydrothermal activity (Pritchard & Simons 2004), slow edifice subsidence (Ebmeier *et al.* 2010) and lava flow contraction (Stevens *et al.* 2001). Regional-scale surveys have detected magma movement at volcanoes previously thought to be quiescent (e.g. on the East African

Rift: Biggs *et al.* 2009) and at locations not obviously associated with a particular volcanic edifice (e.g. the central Andes: Pritchard & Simons 2004).

However, the global distribution of InSAR measurements of volcano deformation is currently uneven, due, in part, to the differences in radar returns from different types of land surface. The majority of radar satellites have operated at C-band wavelengths,  $\lambda = 5.6$  cm, which are known to be affected by vegetation cover. This is a particular problem in the tropics where dense, rapidly growing evergreen vegetation is especially prevalent and causes a high rate of change in surface scatterer properties and therefore rapid decorrelation. This has presented significant obstacles for some C-band studies of volcano deformation in the

tropics (Zebker *et al.* 2000; Stevens & Wadge 2004; Pinel *et al.* 2011). In recent years, this problem has been addressed to some extent with the launch of the Japanese satellite, ALOS, in 2006, which operates at L-band ( $\lambda = 23$  cm) wavelengths. L-band radar penetrates dense vegetation so that the radar returns come from more stable scatterers on the ground surface. ALOS (Advanced Land Observing Satellite) data have allowed the first InSAR measurements at many volcanoes in the Caribbean, northern Andes, Indonesia and Central America (Biggs *et al.* 2010; Ebmeier *et al.* 2010; Fournier *et al.* 2010; Parks *et al.* 2011; Philibosian & Simons 2011). Nonetheless, since the C-band archive stretches back to 1993 while ALOS was only launched in 2006, heavily vegetated volcanoes, many of which are in the tropics, have been understudied relative in drier regions.

Many of the world's active volcanoes are in the tropics and have little or no coverage by ground-based geodetic measurement (e.g. Fournier *et al.* 2009), so that InSAR observations may be the only available method for assessing and monitoring their geodetic activity and the related volcanic hazard. It is therefore important from both hazard mitigation and satellite design perspectives to quantify the applicability of InSAR to tropical volcanoes.

In this study we explore the factors that affect the measurement of volcano deformation in the tropics using InSAR, drawing on examples from an L-band survey of the Central American Volcanic Arc (CAVA) between 2007 and 2010. Some of these factors apply globally (e.g. DEM quality) while others (water vapour variations, vegetation) are of particular concern at tropical volcanoes. We start by discussing the most significant issue, namely stratification and the variability in tropospheric water vapour concentration (see the section on 'Tropospheric water vapour' later), which creates artefacts over topographical peaks. Although such atmospheric artefacts are found at volcanoes across a wide range of latitudes, the significantly greater variability in water vapour concentrations in the tropics make them an extreme case. We then go on to discuss artefacts associated with use of global DEMs and with geometric distortion effects. We also describe patterns in phase decorrelation rates across the arc (see section on 'Coherence in Central America', later), and discuss their relationship to vegetation indexes and land-use classifications, and compare the usefulness and coherence of C-, L- and X- band SAR for a case study volcano, Arenal. The significance of the lack of observations of volcano deformation in Central America in relation to uncertainties in InSAR measurement and to tectonic setting is beyond the scope of the current study and is the focus for future work (Ebmeier *et al.* in prep.).

## InSAR

Repeat pass InSAR produces maps of phase change (interferograms) between two time-separated radar images from which the movement of the ground can be measured on the scale of millimetres to tens of centimetres (Massonnet & Feigl 1998; Bürgmann *et al.* 2000). Phase shifts in an interferogram are caused by changes to satellite viewing geometry (satellite position and relative rotation of target between acquisitions,  $\Delta\Phi_{\text{spatial}}$ ), instrument thermal noise ( $\Delta\Phi_{\text{thermal}}$ ), radar path through the atmosphere ( $\Delta\Phi_{\text{atm}}$ ) and backscatter from the ground surface. Changes at the Earth's surface capable of introducing phase shifts to an interferogram include deformation ( $\Delta\Phi_{\text{def}}$ ), systematic changes to dielectric properties (e.g. due to moisture or thermal expansion/contraction,  $\Delta\Phi_{\text{ground}}$ ) and changes to scattering properties within a pixel ( $\Delta\Phi_{\text{pixel}}$ ). The scattering properties of a pixel are determined by the combination of radiation reflected or scattered from numerous objects, so that it has the appearance of random noise and cannot be predicted in practice.

$$\Delta\Phi = \Delta\Phi_{\text{spatial}} + \Delta\Phi_{\text{thermal}} + \Delta\Phi_{\text{atm}} + \Delta\Phi_{\text{def}} + \Delta\Phi_{\text{ground}} + \Delta\Phi_{\text{pixel}}. \quad (1)$$

Interferometric measurement of surface deformation ( $\Delta\Phi_{\text{def}}$ ) is possible either when other sources of phase shift are relatively small or are constant over large areas.

The coherence of a pixel is usually described in terms of interferometric correlation ( $\hat{\gamma}$ ), which is defined for each pixel using the phase values of both images ( $y_1$  and  $y_2$ ) across a square of at least  $3 \times 3$  pixels (Equation 2). A value of 1 indicates identical phase for all pixels. When interferometric coherence tends to 0, each pixel response is independent (Seymour & Cumming 1994; Hanssen 2001):

$$|\hat{\gamma}| = \frac{|\sum_{n=1}^9 y_1^{(n)} y_2^{*(n)}|}{\sqrt{\sum_{n=1}^9 |y_1^{(n)}|^2 \sum_{n=1}^9 |y_2^{(n)}|^2}}. \quad (2)$$

Interferometric decorrelation is caused by changes in satellite position (geometric decorrelation), instrument properties (thermal decorrelation) and in surface scatterer characteristics (temporal decorrelation) (for further details see Zebker & Villasenor 1992). Geometric decorrelation occurs where the radar wavelength is less than the difference in path length between radar returns from opposite sides of a pixel, and is most pronounced at large baselines. Thermal decorrelation occurs

when the behaviour of the satellite radar antenna varies over time. Temporal decorrelation is caused by scatterers within a pixel moving or changing their reflective properties. For satellite incidence angles of less than  $45^\circ$ , InSAR is more sensitive to vertical than horizontal changes to scatters, so that surfaces where volume scattering is significant (e.g. forests, dense vegetation) are expected to decorrelate more rapidly with time (Zebker & Villaseñor 1992). Precipitation, wind and ecological processes have all been observed to contribute to temporal decorrelation (Ahmed *et al.* 2011).

### **InSAR archive: the Central American Volcanic Arc**

The Central American Volcanic Arc stretches over 1100 km from northern Guatemala, through El Salvador and Nicaragua to central Costa Rica, and is associated with the subduction of the Cocos Plate beneath the Caribbean Plate (Fig. 1). It is made up of 72 volcanoes, spaced at an average of approximately 25 km along the arc (Carr 1984), of which 26 are historically active.

Interferograms were produced from ALOS data between 2007 and 2010. All interferograms were constructed using the Repeat Orbit Processing software (ROI PAC) developed at Caltech/JPL (Rosen *et al.* 2004) with topographical correction made using NASA's Shuttle Radar Topography Mission (SRTM) 90 m DEM. Unwrapping was carried out using a branch-cut algorithm (Goldstein *et al.* 1988) with corrections made manually. The volcanoes were covered by an average of 15 ascending interferograms, with a few supplementary descending interferograms constructed where the ascending data were ambiguous (Fig. 1). We were able to make geodetic measurements at 18 (Santa Maria (Santiaguito), Almolonga, Atitlan, Acatenango, Fuego, Pacaya, Santa Ana, Izalco, San Salvador, San Miguel, San Cristobal, Telica, Cerro Negro, Las Pilas, Momotombo, Masaya, Arenal and Poàs) of Central America's 26 active volcanoes and to characterize the associated uncertainty for each.

### **Tropospheric water vapour**

#### *Water vapour characteristics*

In order to convert the observed phase changes to measurements of displacement, it is assumed that radar propagates at a constant velocity. This would be reasonable for free space, where phase is dependent only on radar wavelength and path length, but introduces errors where there are significant spatial and temporal heterogeneities in the atmosphere. The effective path length actually depends on

temperature, pressure and partial pressure of water vapour between satellite and ground surface, and is separated into 'wet' and 'hydrostatic' delays, caused by water vapour and hydrostatic pressure respectively (Bevis *et al.* 1992; Hanssen 2001). Water vapour artefacts in interferograms depend on the difference between atmospheric conditions on the two dates when Synthetic Aperture Radar (SAR) data were acquired. Variations in water vapour (e.g. 10 cm path delay for a 20% change in relative humidity) are expected to produce larger path delays than hydrostatic pressure (2.3 mm path delay expected for change from 0.5 to 1 mb) (Zebker *et al.* 1997).

The spatial and temporal characteristics of the atmospheric artefacts depend on the distribution of water vapour in the troposphere. Where water vapour is mixed turbulently, it exhibits spatial correlation over length scales typically of the order of 10 km (e.g. Hanssen 2001; Jónsson *et al.* 2002; Lohman & Simons 2005), shows minimal or no correlation with topography and has a typical variability of 1 cm (e.g. Pritchard & Simons 2004). Large, steep volcanoes are commonly associated with both local turbulence on much smaller spatial scales and systematic features in atmospheric mixing caused by high topography (e.g. Webley *et al.* 2004).

Vertically stratified water vapour in the troposphere results in low-magnitude slant range path delays over high topography and higher, more variable path delays over low topography (e.g. Pavez *et al.* (2006)). The resulting artefacts in an interferogram correlate with topography, and appear as concentric fringes around topographical peaks (Fig. 2). As we may expect volume change of a sub-edifice magma chamber to produce a similar phase pattern, centred over the volcanic edifice (e.g. as observed at Etna: Massonnet *et al.* 1995; Beauducel *et al.* 2000), it is particularly difficult to distinguish between these two effects.

In equatorial zones, seasonal variations in water vapour are largely controlled by the north-south migration of the intertropical convergence zone (ITCZ), producing some of the greatest variations in water vapour globally. Radar path delays of up to 11, 8 and 6 cm have been measured at Mount Cameroon (Heleno *et al.* 2010), Sakurajima, Japan (Remy *et al.* 2003), and Soufrière Hills, Montserrat (Wadge *et al.* 2006), respectively (Table 1).

#### *Identification of atmospheric artefacts*

Characteristic features of atmospheric phase artefacts include: (a) a correlation between topography and phase (for stratified water vapour); (b) an association of the signal with particular acquisition dates; and (c) either the lack of any dependence on time (turbulent water vapour) or a seasonal dependence (stratified water vapour) of signal

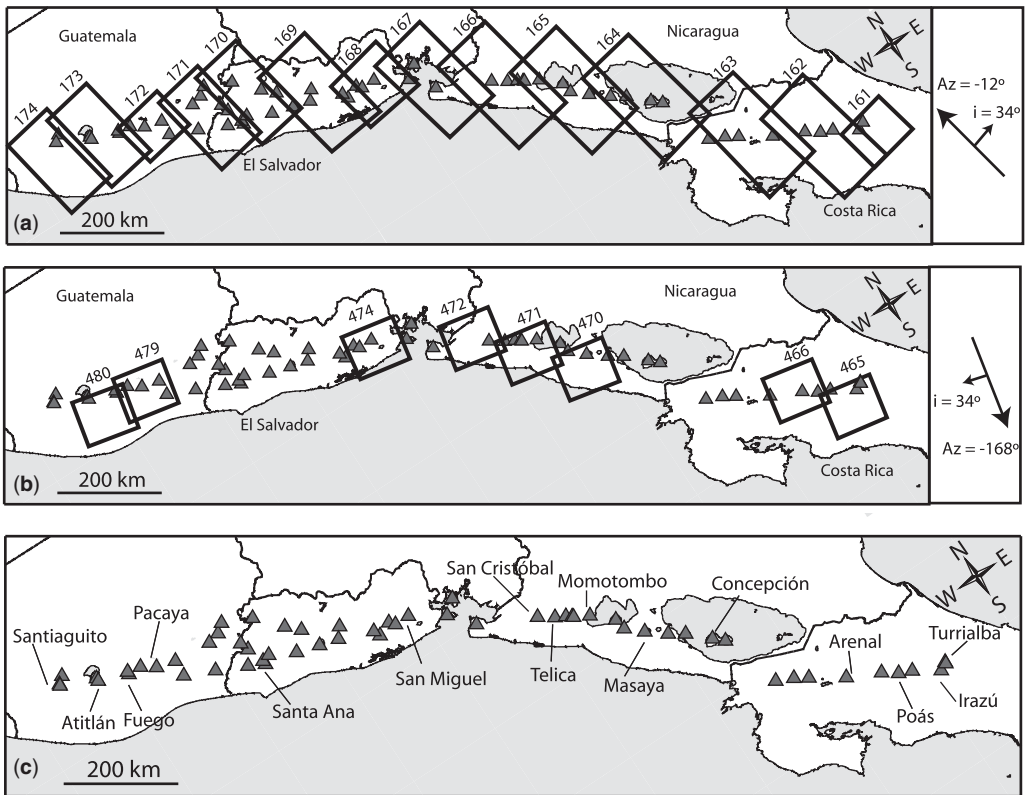


**Fig. 1.** (a) Ascending ALOS data used in arc-scale study of Central American Volcanic Arc. Black boxes show the track locations and extent of our data, and triangles show volcano locations. (b) Descending ALOS data used to complement ascending data where possible. (c) Map showing the locations of the volcanoes mentioned in this study.

magnitude (Fig. 3). Water vapour artefacts are identified using a combination of these properties, as well as through the use of independent atmospheric data or models (examples from the literature are shown in Table 1).

A correlation between height of topography and phase in an individual interferogram is indicative of the presence of water vapour (e.g. Fig. 4) but is not necessarily diagnostic. The injection or drainage of a body of magma within or just below a volcanic edifice could conceivably create a similar pattern in phase. However, where a number of topographical peaks in the same interferogram show similar phase patterns, they are most probably caused by atmospheric delay.

Analysis of the temporal development of phase through a set of interferograms provides further evidence to distinguish between atmospheric artefacts and true deformation. The method of 'pair-wise logic' (e.g. Massonnet & Feigl 1995) compares pairs of interferograms that have a common date in master and slave positions. If artefacts of a

similar magnitude and spatial pattern but opposite sign appear, then the artefact can be associated with the SAR acquisition date held in common. Two examples of such pairs from Momotombo Volcano, Nicaragua are shown in Figure 5. Although this method had the advantage of simplicity, it is only reliable where atmospheric conditions are relatively stable and unusual phase delays are associated with a small number of acquisition dates.

At the sampling rate of a satellite repeat intervals, we expect the temporal signal of atmospheric water vapour to be either structureless, with a random variation in phase between relatively constant bounds, or to vary with the period of a year as a function of seasonal variations in water vapour (e.g. Heleno *et al.* 2010). Creating time series of interferometric phase (e.g. Lundgren *et al.* 2001; Bernardino *et al.* 2002) is a useful tool when dealing with situations where atmospheric effects seem to dominate the majority of interferograms. Long-term, steady-rate deformation may be detectable in this way (e.g. Ferretti *et al.* 2001), but

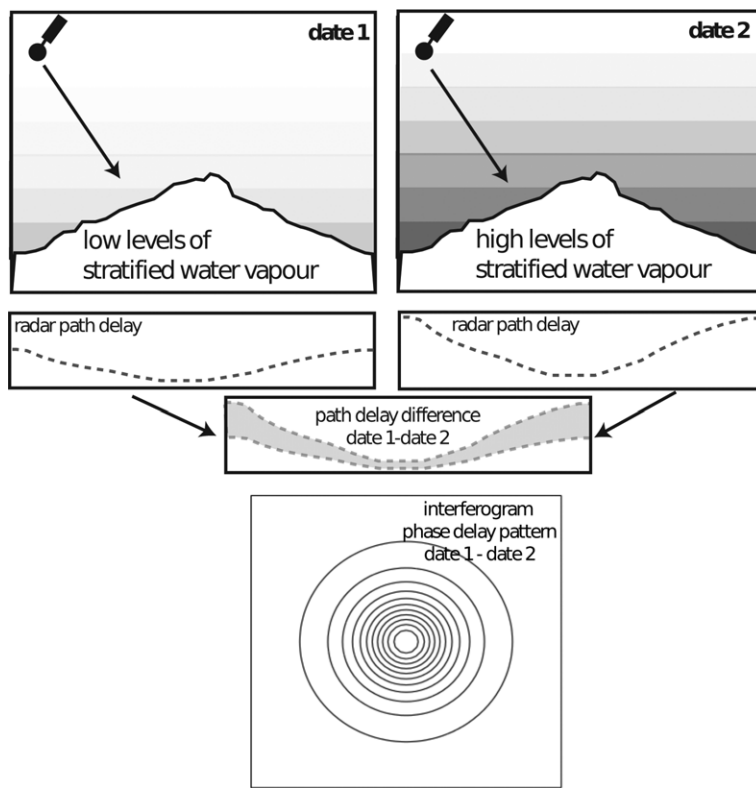


**Fig. 2.** Cartoon illustrating the generation of a topographically correlated phase delay due to variations in concentration of stratified water vapour. Typical values for peak phase delay range from 1 to 5 cm (2 cm would indicate *c.* 5% change in relative humidity).

reversible deformation (where net deformation over longer time-span interferograms will be zero, as the ground returns to its original position) may be missed.

InSAR only provides relative measurements, as phase changes are always found relative to a reference point. While for volcanoes it is generally possible to select a reference far away from any deformation source, it is very difficult to avoid the effects of local atmospheric variation. If a reference pixel is selected over an area where atmospheric variation differs to that over the volcano, local differences in atmospheric delay are likely to dominate time series and mask any deformation.

We avoid this problem by referencing our interferograms to the average value of phase within an annulus centred on the volcano, thus minimizing the impact of small-scale variations in atmospheric noise in other parts of the interferogram on our time series. Reference annuli typically had inner radii of 2–6 km (large enough to encompass entire edifice and surrounding topographical features) and outer radii with limits defined by either the

edge of the interferogram or (more commonly) the limit of the continuously coherent area. The difference between the mean height of topography within this area and the volcano summit was generally close to the volcano edifice height.

#### *Water vapour in Central America*

We use the characteristic properties described above and the processes outlined in Figure 3 to identify atmospheric water vapour in the Central American dataset. We constructed time series for active volcanoes in Central America using a linear least squares inversion of the phase changes from a network of interferograms (e.g. Lundgren *et al.* 2001; Schmidt & Bürgmann 2003). Inversion was carried out with a generalized inverse matrix using singular value decomposition and solving for velocity (e.g. Berardino *et al.* 2002), rather than displacement, to avoid unrealistic discontinuities. This problem is commonly rank deficient where there are subsets of interferograms that do not hold an acquisition in common. We therefore solve for velocity relative

**Table 1.** Selected literature examples of the identification and/or mitigation of water vapour signals over volcanoes

Volcano	Maximum magnitude of atmospheric delay (cm)	Volcano height (m)	Explicit means of identification as stratified water vapour	Mitigation method	Reference
Mount Cameroon	11	4095	Phase–elevation correlation and seasonal correlation with MODIS and GPS water vapour measurements	–	Heleno <i>et al.</i> (2010)
Sakura jima	8	1117	Phase–elevation correlation	Network adjustment based on phase–elevation relationship	Remy <i>et al.</i> (2003)
Soufrière Hills	6	915	Implicit in correction	GPS water vapour correction	Wadge <i>et al.</i> (2006)
Popocatepetl	7	5426	Comparison to predicted delay from meteorological model	Correction of unwrapped phase with model delay	Pinel <i>et al.</i> (2011)
Colima	17	3850	Comparison to predicted delay from meteorological model	Correction of unwrapped phase with modelled delay	Pinel <i>et al.</i> (2011)
Etna	c. 6	3330	Comparison with atmospheric model	Correction from high-resolution atmospheric model	Wadge <i>et al.</i> (2002, 2010)
Hualca Hualca	4	5967	Pair-wise logic, time independence	–	Pritchard & Simons (2004)

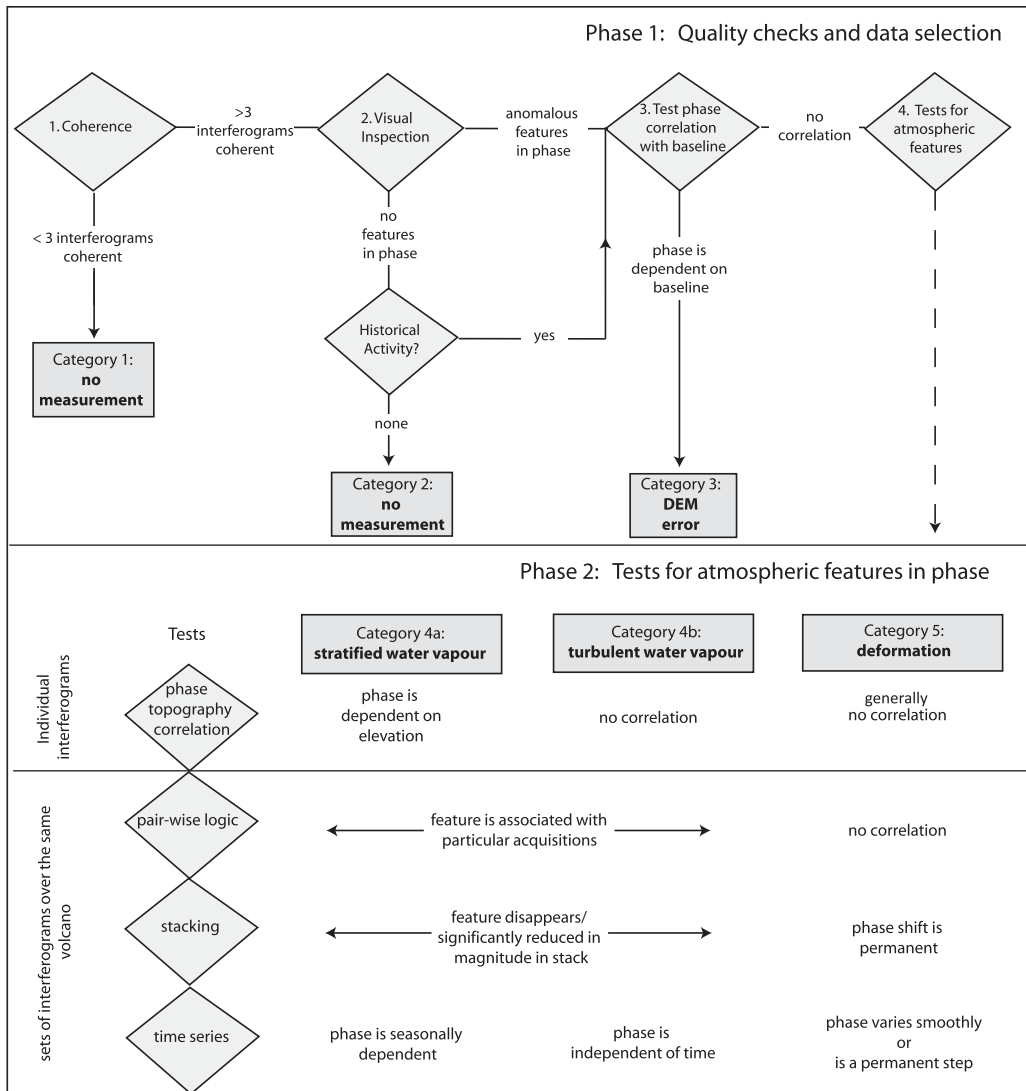


**Fig. 3.** Flowchart illustrating the process of analysing InSAR phase delays to: (a) Phase 1 – check the data for quality; and (b) Phase 2 – distinguish between atmospheric and deformation features.

to the first date, which we explicitly define as showing no deformation.

We find the root mean squared (r.m.s.) variation of the time series after the removal of any linear trend. The r.m.s. variation of the remaining signal is used as an indicator of the average magnitude of atmospheric delay at each volcano, and will not be affected by steady deformation signals at any volcanoes that are deforming (e.g. Arenal). The residual appears random with no systematic seasonal or similar trend. Root mean squared variation shows a linear relationship with the difference in

topographical height between the edifice and the mean height of the reference annulus (Fig. 6). Excluding one outlier (Santa Ana, El Salvador) the time series r.m.s. variation increases with height difference between the edifice and reference annulus with a best-fit gradient of 2 cm/km height difference (Fig. 6). The high value at Santa Ana is thought to be associated with an unusually large topographically correlated phase in one interferogram (Track 171, 9 March–9 September 2009) and the removal of this interferogram from the time series reduces r.m.s. variation at Santa Ana to

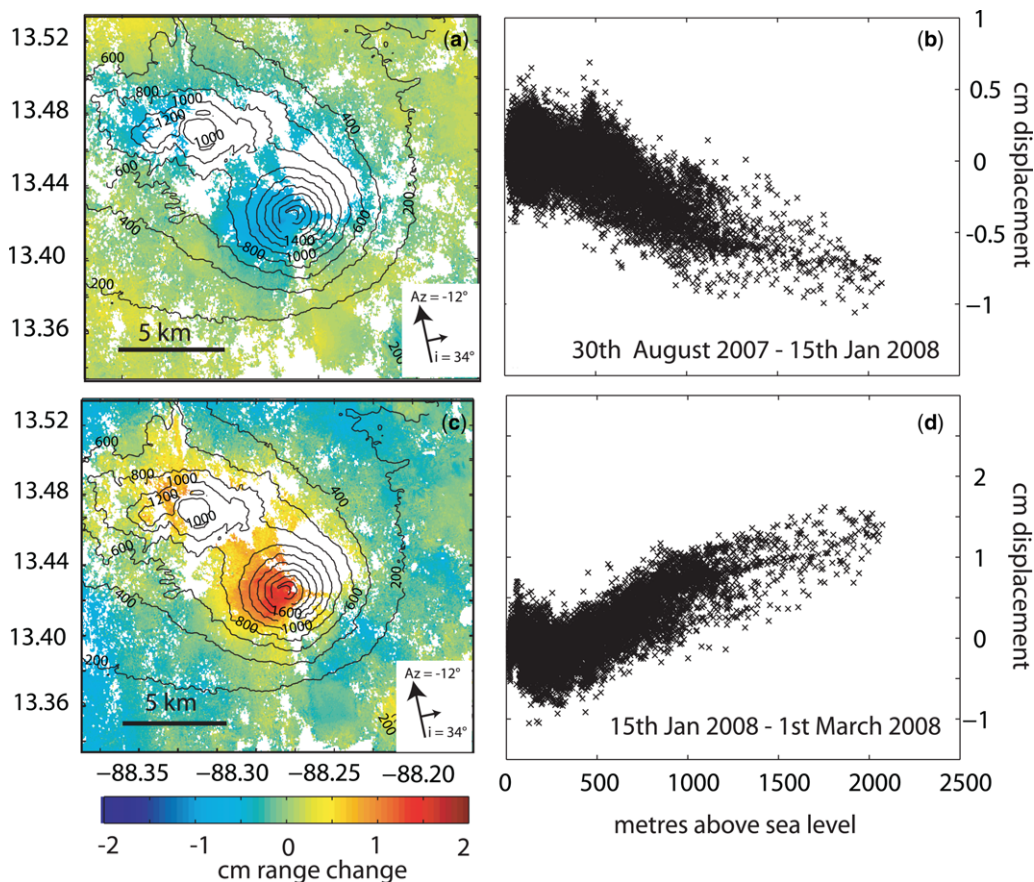


**Fig. 4.** Two interferograms (a & c) of San Miguel, El Salvador sharing a common date and their associated plots of range change against topographical height (b & d) on the edifice.

3.8 cm, well within the normal distribution. There are no similar features in other interferograms for Santa Ana, and the time series is otherwise very similar to that for nearby cinder cone Izalco (just under 5 km south of Santa Ana).

This relationship between volcano edifice height and magnitude of atmospheric phase artefact has implications for the uncertainties of InSAR measurements at different volcanoes. For transient deformation (taking place over a period greater than the satellite repeat time) to be distinguishable from normal atmospheric variation at a volcano of edifice height exceeding 2000 m (e.g. Fuego), it must exceed about 4 cm, while we may be able to detect much lower magnitude deformation (>1 cm) at low-relief volcanoes (e.g. Masaya). Although not possible with this dataset, if the interferograms were limited to those from the same season (e.g. winter–winter or summer–summer),

we hypothesize that the relationship between topographical height and atmospheric variation might be weaker.

#### *Potential for mitigation of atmospheric effects*

Several methods have been proposed (such as stacking, empirical corrections, external data and models) by which atmospheric artefacts can be reduced or removed (e.g. Hanssen 2001; Remy *et al.* 2003; Li *et al.* 2005, 2006; Wadge *et al.* 2006). In this subsection, we outline each method and assess its applicability to the volcanoes of Central America.

As turbulent water vapour artefacts are essentially random in time, stacking a set of interferograms together will increase the signal to noise

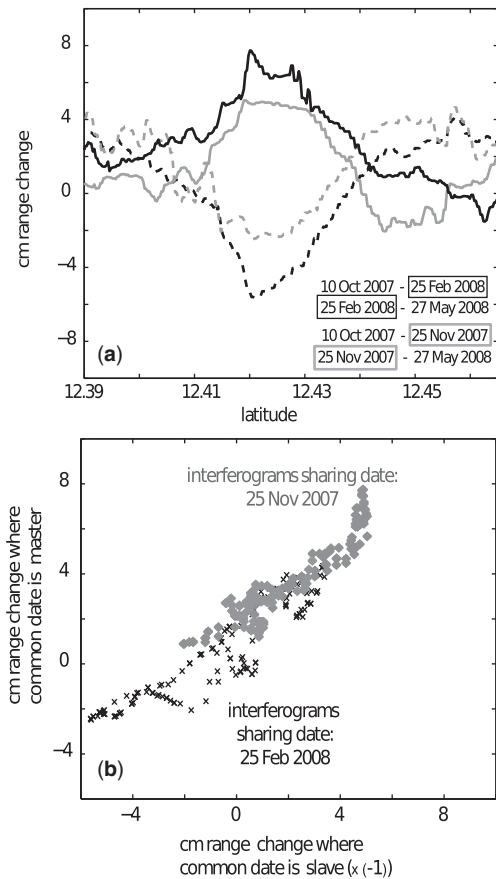


**Fig. 5.** (a) North–south LOS range–change transects through a pair of interferograms from Momotombo Volcano, Nicaragua. The fact that these lines are very close to being mirror images shows that the largest contribution to phase is associated with the date held in common and reflects an atmospheric artefact. Lines of the same shade hold an acquisition date in common. (b) Scatter plot of phase from the interferogram where common date is the master against  $(-1)$  phase from the interferogram where common date is slave.

ratio. For deformation of a constant rate, a standard stack composed of  $N$  interferograms of equal time span will increase the signal noise ratio by  $\sqrt{N}$ , whereas a chain stack (where interferograms span consecutive periods of time) will increase the signal to noise ratio by a factor of  $N$ , as the atmospheric components on each slave image will cancel with the master of the subsequent image (Biggs *et al.* 2007). However, the improvement in signal to noise ratio is achieved at a loss of temporal resolution, and is therefore better suited to studying long-term rather than transient volcano deformation events.

Empirical corrections for stratified water vapour can be made on the basis of correlations between phase and topography. This is most robust for very large datasets with high temporal repeatability, so that analysis of phase–topography correlations for a set of interferograms can be used to make adjustments to the network of interferograms (e.g. Beauducel *et al.* 2000; Remy *et al.* 2003). Alternatively, where the area of deformation is already well constrained by other data sources, topographically correlated fringes can also be removed from individual interferograms by solving for a best-fit relationship with topography, sometimes treated as linear (e.g. Wicks *et al.* 2002), but shown to be better approximated by a non-linear model for steep volcanoes (Remy *et al.* 2003). Recent studies have used band-pass decomposition (Lin *et al.* 2010) and wavelet analysis (Shirzaei & Bürgmann 2012) to find the relationships between topography and phase for different components of an interferogram.

Other approaches applied to correcting the effects of water vapour phase delays over volcanoes require direct measurements of water vapour, ideally coincident with SAR acquisitions. These include GPS measurements of water vapour (Wadge *et al.* 2002, 2006) or satellite-based measurements (e.g. MODIS: Li *et al.* 2005; Pavez *et al.* 2006). Calculation of phase delay directly from empirical water vapour and hydrostatic pressure values requires a high spatial density (limited for ground-based instruments) and high temporal density (limited for satellite instruments) of measurements in order to provide a useful correction. A low density of measurements creates particular difficulties where the water vapour field is highly dynamic, as is the case in the tropics. High-resolution weather models have been used successfully to correct for atmospheric water vapour at Etna and over Hawaii (Webley *et al.* 2004; Foster *et al.* 2006; Wadge *et al.* 2006) but, so far, have only been applied over limited areas, where local atmospheric physics is well understood.

In the absence of high densities of ground-based atmospheric measurements for calibration and an understanding of the dynamic weather systems around individual volcanoes, regional InSAR surveys of volcano deformation such as this are generally unsuitable for correction of atmospheric artefacts. Meteorological reanalysis data (e.g. Fournier *et al.* 2011; Jolivet *et al.* 2011) has been used to remove atmospheric contributions on a regional scale, but the low spatial resolution of weather data available makes this approach more suitable for retrieving longer wavelength interseismic deformation than the deformation of volcanoes. Empirical atmospheric corrections from an assumed relationship with topography are particularly likely to

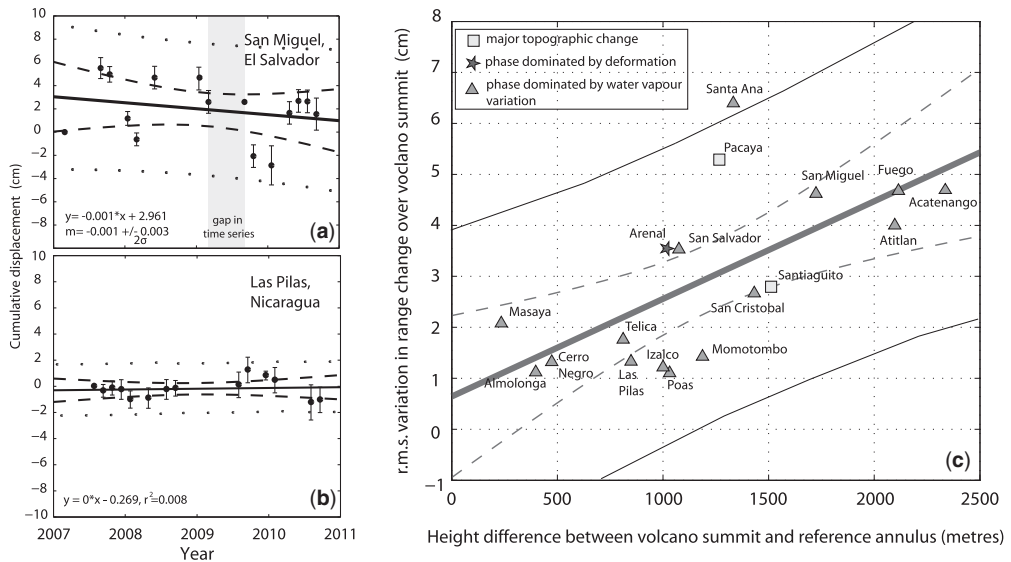


**Fig. 6.** (a) Time series of phase over the edifice of San Miguel, El Salvador (summit 2130 m a.s.l.) and (b) Las Pilas, Nicaragua (1088 m a.s.l.). Error bars show the standard deviation of 100 Monte Carlo repetitions of the inversion with randomly generated, non-spatially correlated noise of amplitude 1 cm added to each interferogram. (c) Plot of the r.m.s. variation in detrended time series for active volcanoes (Fig. 1) as a function of the height different between volcano summit area and the average topographical height of the reference annulus. The thick solid line shows the line of best-fit, the dotted line shows the 95% confidence envelope for the gradient, and the thinner solid line in (c) and dots in (a) and (b) show the 95% confidence envelope for any individual point.

introduce artefacts or to remove elements of any masked deformation signal. They are most appropriate where the nature of the expected deformation signal is known from other sources. Therefore, we did not attempt to remove water vapour variations from any of the Central American data.

### Limitations of global DEMs and mitigation

Digital elevation models are used to correct for the change in path length associated with the satellite position between acquisitions. Errors or gaps in the DEM propagate into the interferogram, creating phase shifts ( $\Delta\Phi_{\text{topo}}$ ), which are proportional to the satellite perpendicular baseline ( $B_{\text{perp}}$ ), and inversely proportional to radar wavelength ( $\lambda$ ), incidence angle ( $\theta_i$ ) and range of satellite from the ground ( $r$ ) (e.g. Rodriguez & Martin 1992; Zebker & Villasenor 1992):

$$\delta\phi_{\text{topo}} = \frac{4\pi B_{\text{perp}}}{r\lambda \sin \theta_i} \delta z. \quad (3)$$

Such topographical phase changes can be identified by examining the relationship between phase ( $\Delta\Phi$ ) and perpendicular baseline ( $B_{\text{perp}}$ ) for a set of interferograms, and can be the result of a change

in topography since the DEM data were acquired (e.g. fresh lava flows emplaced since the DEM's acquisition; Ebmeier *et al.* 2012) or an error in the DEM itself (Fig. 7b, c). For the same perpendicular baselines, topographical artefacts would be greater for C-band than L-band data but, in practice, the baselines for ALOS are generally much larger than for Envisat, and will produce greater topographical errors.

Over much of the world the only DEMs available for InSAR processing are global datasets derived from satellite data, such as NASA's Shuttle Radar Topography Mission (SRTM) 90 m DEM and the Advanced Spaceborne Thermal Emission and Reflection Radiometer (ASTER GDEM). The SRTM DEM (Rosen *et al.* 2001) was acquired from a single-pass InSAR instrument on an 11 day shuttle mission in February 2000. Errors in height from SRTM data are made up of uniformly distributed, small systematic errors due to shuttle motion (>2 m) and spatially variable medium to short wavelength errors, particularly over steep topography (2–10 m) (Rodriguez *et al.* 2006). These errors are larger and more common both at lower latitudes, where fewer data were collected, and over high topographical relief, where geometric decorrelation in phase (see the 'InSAR' subsection earlier in this paper) has most impact (Rodriguez

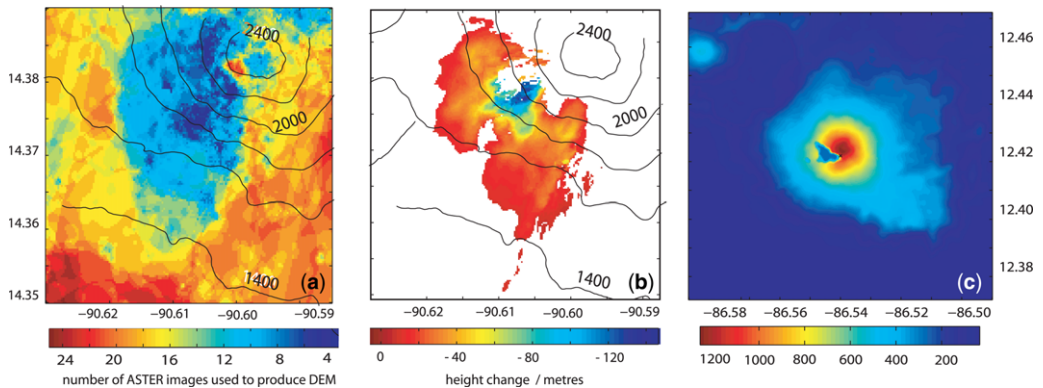


**Fig. 7.** (a) The number of ASTER images used to determine topographical height over Pacaya Volcano, Guatemala for each pixel. Data are not used when the ground is obscured by cloud or by the volcanic plume. (b) Map of DEM error calculated from topographical phase changes in a set of interferograms corrected using the ASTER GDEM. (c) Data gap near the summit of Momotombo, Nicaragua, SRTM 90 DEM. Similar features are found in both the SRTM and GDEM. Interpolation of such gaps generally do not result in DEM errors in interferograms.

*et al.* 2006). The volcanic arc in Central America falls into both of these categories, and can be expected to have errors of the order of 10 m, which correspond to path length artefacts of magnitude 0.5–2 cm for ALOS interferograms (typical baselines 500–2000 m).

The ASTER GDEM (Reuter *et al.* 2009) was constructed from Aster band-3 near-infrared imagery. DEMs are produced from the 10 year archive of stereo-pairs of ASTER images, cloud-covered areas are masked out and the DEMs are stacked; the final ASTER GDEM records the best-fit topography for the non-cloudy images. The average r.m.s. error in GDEM heights is 18–29 m (Reuter *et al.* 2009). The largest uncertainties are expected to be in areas of frequent cloud cover where the DEM was constructed from small numbers of ASTER stereo-pairs (e.g. Pacaya: Fig. 7a, b).

For the Central American ALOS data, we used the SRTM DEM, interpolated to a resolution of 30 m. For a few volcanoes where there were issues with the SRTM data or where we expected significant topographical change since 2000, we also compared our results to interferograms corrected using ASTER GDEM. Despite gaps in the SRTM DEM around some volcano summits (e.g. Momotombo, Nicaragua: Fig. 7c), the interpolated version was accurate enough to allow us to process interferograms without introducing artefacts into the phase. However, the GDEM was found to introduce artefacts, presumably owing to the low number of cloud-free images (Ebmeier *et al.* 2012). With enough interferograms and a large enough range of baselines, it may be possible to use Equation (3) to calculate errors in topographical

height with an accuracy sufficient to correct any errors in the DEMs, although this may be limited by poor phase coherence around summit areas where most DEM errors occur.

Both SRTM and GDEM have very low spatial resolutions (90 and 30 m, respectively) compared with new X-band SAR data (3 m), such as that from TerraSAR-X (TSX). These new data will be most useful over small areas where deformation is known to be taking place and a high-resolution local DEM can be acquired.

### Geometric distortion and optimal acquisition strategy

Radar satellites produce images in range and azimuth co-ordinate systems, which, owing to the effects of topography, may be distorted in comparison with ground-based co-ordinate systems (e.g. Fig. 8a–d). Interferograms are reprojected into latitude and longitude (geocoded) using a DEM (e.g. Fig. 8c, d). The extent of the geometric distortions depends on the radar look angle and the steepness of topography, and can cause problems for measurements at steep-sided stratovolcanoes (e.g. Atitlan, Guatemala).

Where the slope is steep, but the angles is less than the satellite look angle, the side of a volcano facing the satellite becomes foreshortened – the geocoded pixel size is smaller on the far side of volcano than the near side. For slope angles exceeding the satellite look angle, returns from the top of the slope will arrive before those at the bottom (layover: Fig. 8e) and parts of the far side of the

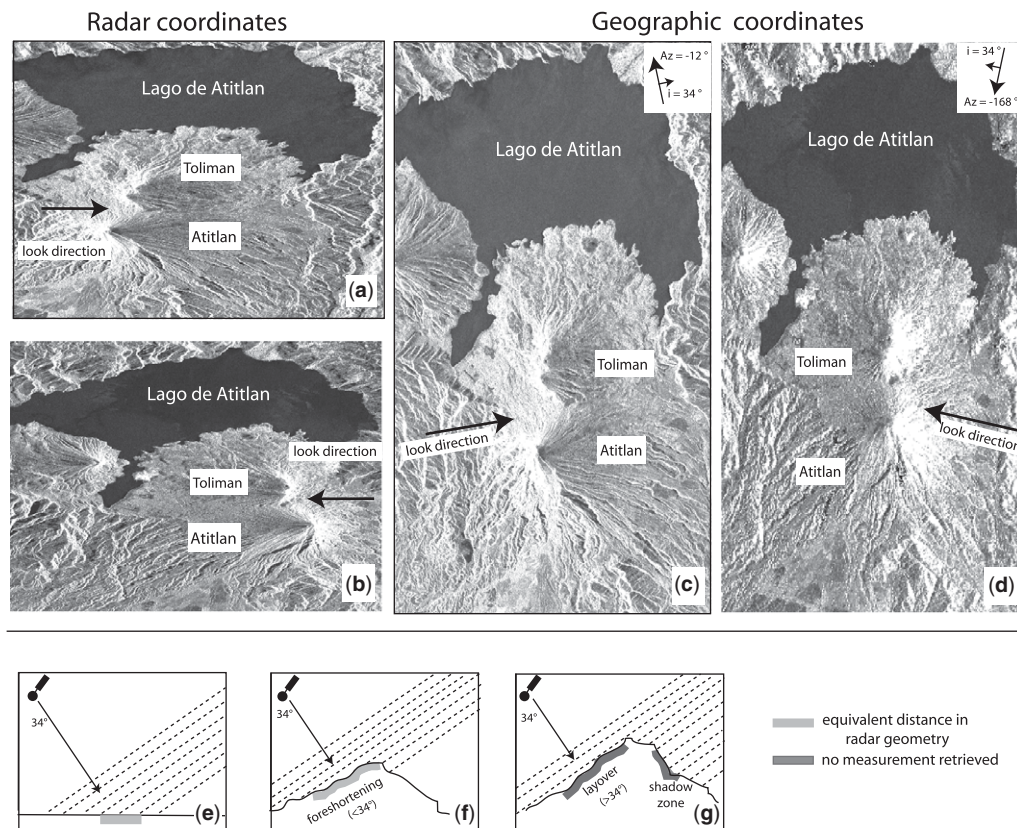


**Fig. 8.** (a) Example of an amplitude image of the Atitlan and Toliman volcanoes in ascending radar geometry (b) Amplitude image of Atitlan and Toliman in descending radar geometry. (c) Ascending amplitude image reprojected into latitude and longitude showing foreshortening of the western slope. (d) Descending amplitude image in latitude and longitude showing foreshortening of the eastern slope. (e)–(g) Cartoons showing the conditions that lead to foreshortening, layover and shadow, when volcano slopes exceed the satellite look angle. The satellite is moving into the page in each instance, the arrow shows the satellite line of sight and the dotted lines indicate points of apparently equal distance from the satellite.

volcano will not produce a radar return (shadowing). At some of the steepest volcano summits in Central America we observe a layover and shadow effects (e.g. Fuego or Atitlan, Guatemala). In this case there can be no correction and data for that section of the volcano cannot be used. Foreshortening and layover will also have an effect on coherence as the radar potentially samples a much greater area of the ground, effectively increasing the pixel ‘size’ (see Fig. 8f).

To ensure that there is good resolution on all parts of steep volcanic edifices, it is necessary to have images from both ascending and descending paths. Many deformation signals are isolated to only one part of a volcanic edifice. For example, Fournier *et al.* (2010)’s analysis of ascending data over a large proportion of Latin America did not

show up asymmetrical gravity-driven deformation at Arenal, Costa Rica (Ebmeier *et al.* 2010), which is only clearly observable in descending interferograms. Furthermore, since InSAR only measures displacement along the satellite line of sight, any motion perpendicular to this vector will not be detected and images from both look directions are required to determine the direction of the vector displacement.

In Central America, the majority of acquisitions made were on ascending passes due to JAXA’s acquisition strategy but, for this study, we were able to produce at least one descending interferogram over almost all currently active volcanoes (see Fig. 1a, b). For steep-sided volcanoes, acquisition strategies incorporating both ascending and descending tracks are particularly advantageous.

## Coherence in Central America

The poor radar penetration of dense tropical vegetation using widely used SAR instruments (e.g. ERS, ASAR and ENVISAT) has been the primary factor limiting InSAR measurements in many parts of the tropics. The effect of vegetation on InSAR is dependent on wavelength, with L-band radar ( $\lambda = 23$  cm) maintaining coherence much better than C-band radar ( $\lambda = 5.6$  cm). The relative coherence between two interferograms showing the same part of the ground will depend on numerous factors in addition to SAR wavelength, including time spanned, perpendicular baseline, differences between surface scatterers and different rates of instrument-related decorrelation (e.g. Zebker & Villasenor 1992; Hanssen 2001). As interferometric correlation ( $\gamma$ ) is estimated from phase values for a set of neighbouring pixels (Equation 2), pixel dimensions are also important. In addition, choices made during InSAR processing, such as spatial wavelength of filtering and degree of multilooking (reduction of spatial resolution with the aim of increasing the size of a coherent area), will also affect our estimations of correlation. Owing to the nature of the estimator used to examine interferometric correlation (Equation 2), areas that are entirely incoherent will still produce an apparent coherence value. We therefore use empirically derived 'threshold' coherence when comparing the coherence of interferograms processed to different number of looks (multilooking consists of taking a weighted average of neighbouring complex pixels: the greater the number of looks, the lower the spatial resolution) in the subsection 'SAR wavelength comparison: Arenal, Costa Rica' later.

We use the data from our arc-scale survey, outlined in Figure 1, to examine patterns of interferometric coherence in Central America. As this is all L-band ALOS data, processed in the same manner, comparison between coherence as a function of time and spatial baseline for different areas can be made directly. Of the 26 active volcanoes in the arc, L-band data for just three (Concepción, Irazu and Turrialba) were too incoherent to make any measurement of deformation at all. Measurements are restricted at other volcanoes, however, by high rates of decorrelation, which meant that only short temporal baseline interferograms could be constructed. Making the distinction between water vapour signals and deformation often requires enough interferograms to examine the temporal development of the phase, so this hampers our analysis. It also imposes spatial limitations on our measurements. At Arenal (see the 'SAR wavelength comparison: Arenal, Costa Rica' subsection), for example, coherence is limited to the stable surfaces of young lava flows (Ebmeier *et al.* 2010). This

confined our measurement to a 2.5 km<sup>2</sup> region on the western side of the volcano, making the measurement of any longer wavelength deformation impossible. The summits of volcanoes with continuous or semi-continuous explosive activity, such as Santiaguito, Fuego, Pacaya (Guatemala) or Arenal (Costa Rica), were also consistently incoherent.

We investigate the relative importance of the contributions of geometrical and temporal decorrelation to patterns of coherence across Central America. Unlike the many analytical models for coherence used to measure (e.g. stem volume or tree heights: see, e.g., Balzter 2001; Santoro *et al.* 2002), we do not aim to extract information about ecological processes from InSAR coherence but to predict where InSAR measurements at volcanoes are likely to be useful and where they are most likely to be limited by rapid decorrelation. Temporal decorrelation is generally caused by volcanic activity, slope instability or, sometimes, very rapid changes in vegetation cover (e.g. rapidly developing kill zones at Poás and Turrialba: Martini *et al.* 2010) close to a volcano's summit. The lower flanks of volcanoes in Central America, however, are commonly either covered by rainforest or are intensively cultivated. It is on the lower slopes and surrounding area that we expect to observe any deformation associated with deeper magmatic processes, so understanding the relationship between vegetation cover and decorrelation is useful for understanding limitations on volcano deformation measurement.

### Coherence model

The mean coherence for the complete Central American ALOS data (Fig. 9: data sampled into 0.1° × 0.1° boxes) shows a dependence on both time span of interferogram and perpendicular baseline. After about 200 days, mean coherence has decayed exponentially to a value of about 0.18 compared to a value of 0.3 for interferograms covering the shortest possible time span (46 days). The difference between coherence in the lowest and highest baseline interval is less significant, falling from 0.26 to 0.19.

Mean coherence is not particularly useful as an indicator of whether volcanic edifices will be coherent as they make up a relatively small proportion of a scene by area, and are commonly not representative of the rest of an interferogram. Fresh, young lavas, for example, decorrelate slowly, whereas scattering properties of explosive products alter rapidly, especially when deposited on steep slopes. It is considered possible to use interferometric data where its coherence is above about 0.15, the value used as the threshold for unwrapping routines (e.g. branchcut algorithm: Goldstein *et al.* 1988).

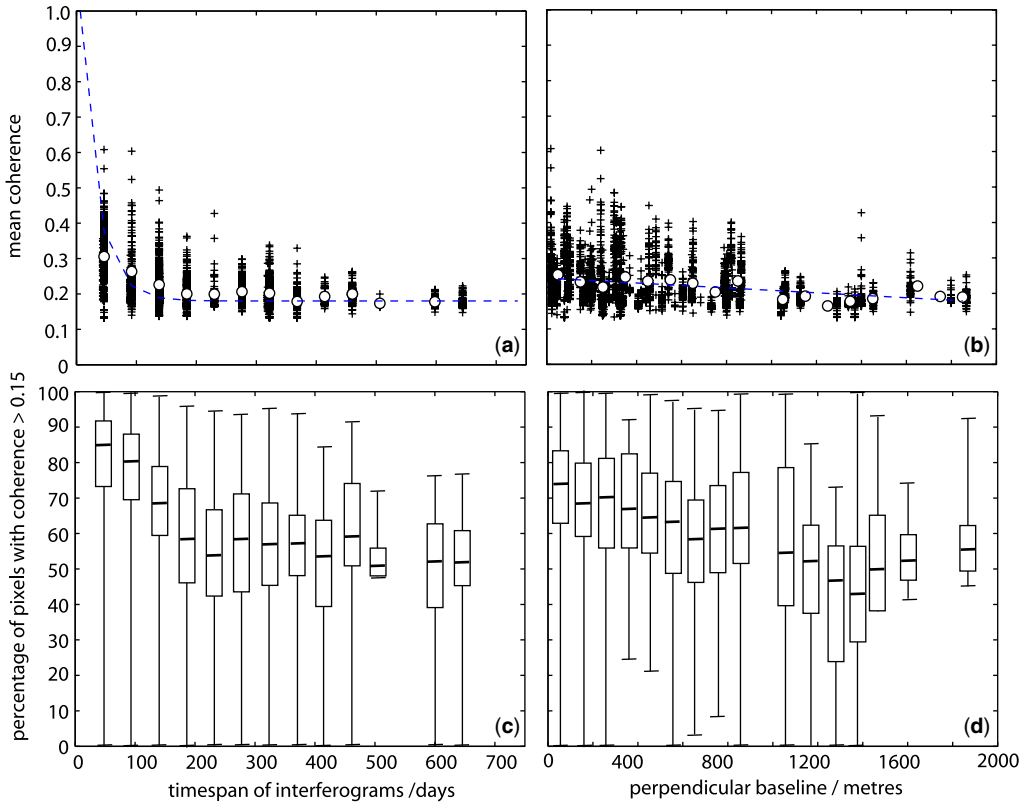


**Fig. 9.** Mean coherence for the whole Central American dataset plotted as a function of (a) time in days and (b) perpendicular baseline. Each point represents the mean value of coherence for a  $0.1^\circ \times 0.1^\circ$  box in an interferogram. The choice of resolution captures regional-scale differences in vegetation and land use. Mean values are marked with circles on (a) and (b). (c) & (d) show box and whisker plots of the percentage of pixels with correlation above 0.15 as a function of time and perpendicular baseline, respectively. The limits of the boxes are the 25th and 75th percentile, while the central black line shows the position of the median. Minimum and maximum values are shown by the extent of the black line.

The percentage of pixels above this threshold coherence and the mean coherence are related, but not directly proportional, as coherences are not normally distributed about the mean value (Fig. 9c, d). The relationships between percentage coherence above 0.15 and time or baseline are therefore not as clear as for mean coherence, but more likely to yield information useful for our purpose of investigating volcano deformation.

We model percentage coherence above 0.15 ( $C$ ) as the product of exponential decay functions describing coherence in terms of time in years ( $t$ ), perpendicular baseline separation ( $B_{\text{perp}}$ ) and a parameter describing seasonal dependence ( $\alpha$ ). For simplicity, we neglect the effects of some instrument-dependent parameters also associated with decorrelation (rotation of satellite look angle and thermal decorrelation, as discussed by Zebker & Villasenor 1992; Hanssen 2001) that we expect

to be smaller than the contributions of geometric and temporal decorrelation. Our choice of exponential decay functions to describe temporal and geometric decorrelation is informed by analytical expressions (e.g. temporal decorrelation: Zebker & Villasenor 1992), and examination of the coherence–temporal baseline relationship and coherence–spatial baseline relationship for our complete dataset (Fig. 9):

$$C = 1 + \frac{1}{\alpha} \left( e^{-\frac{B_{\text{perp}}}{\beta}} e^{-\frac{t}{\tau}} \cos(2\pi t) - 1 \right). \quad (4)$$

The parameters  $\beta$  and  $\tau$  reflect the dependence of coherence on  $B_{\text{perp}}$  and time spanned by the interferogram, respectively. We use non-linear inversion, where the difference between model predicted values and our coherence data were minimized using a least-squares method, to find the values of  $\beta$ ,  $\tau$

and  $\alpha$  that best fit the data. We checked that our results for these parameters were global, rather than local, solutions by varying the starting values for each parameter used in the least-squares method and confirming that our solutions were not affected.

The parameter  $\alpha$  is added to the expression to allow for a seasonal difference in coherence and controls the amplitude of a cosine function with the period of a year, which moderates the shape of the exponential expressions (Fig. 10a, b). This additional parameter was found to significantly improve the fit of our model to the coherence data (e.g. reducing the residual in fit by about 20% in northern Nicaragua, Track 166). A low  $\alpha$  value indicates that coherence has a strong seasonal dependence.

Two examples, expressed as a function of time, are shown in Figure 10a, b. The best-fit solution for Track 172 (Fig. 10a), in central Guatemala, shows slower decorrelation as a function of time and a lesser seasonal dependence than data from Track 166 (Fig. 10b) in northern Nicaragua ( $\tau = 150$  and  $\alpha = 4.9$ , relative to 90 and 2.3). Predicted coherence above the threshold value is calculated from our best-fit values for  $\tau$ ,  $\beta$  and  $\alpha$  for

$0.1^\circ \times 0.1^\circ$  boxes across Central America, and is shown plotted against actual coherence in Figure 10c. The spatial distribution of the r.m.s. misfit between predicted and measured percentage of pixels above threshold coherence is shown in Figure 10d.

The distribution of values of  $\tau$ ,  $\beta$  and  $\alpha$  across Central America is spatially noisy (Fig. 11b–d) but the temporal-dependence parameters ( $\tau$  and  $\alpha$ ) show some trends, which are discussed in the next subsection.  $\beta$ , however, takes very high values across the majority of Central America ( $> 10\,000$ ), showing that geometric factors are largely of lesser significance than time-dependent processes. The remaining lower values of  $\beta$  are, typically, of the order of  $1000\text{--}3000\text{ m}^{-1}$ , show no correlation with topographical height and are mostly isolated to two tracks with some particularly large baseline interferograms (tracks 165 and 162).

### Coherence and land use

Our arc-scale analysis of coherence data shows that time-dependent processes, most probably associated with vegetation growth, dominate decorrelation

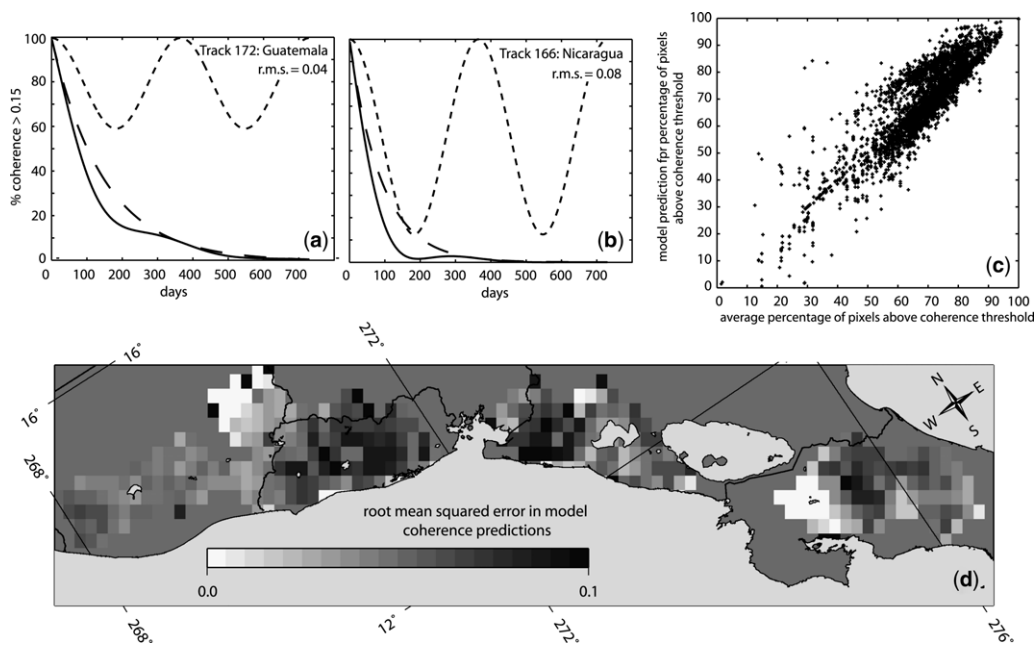


**Fig. 10.** Schematic examples of our simple coherence model for average coherence across (a) Track 172 in Guatemala and (b) Track 166 in Nicaragua (as shown in Fig. 1a). These show model predictions as a function of time only for percentage coherence above a threshold value of 0.15. Black dashed lines show exponential time dependence, finer dashed line shows our approximation of seasonal dependence and solid lines show the combined model. (c) Plot illustrating the fit between average percentage coherence above 0.15 for all our data at a resolution of  $0.1^\circ$  and model predictions for the same value. (d) Map of r.m.s. error in model predictions across Central America, using the same resolution as for Figure 11.

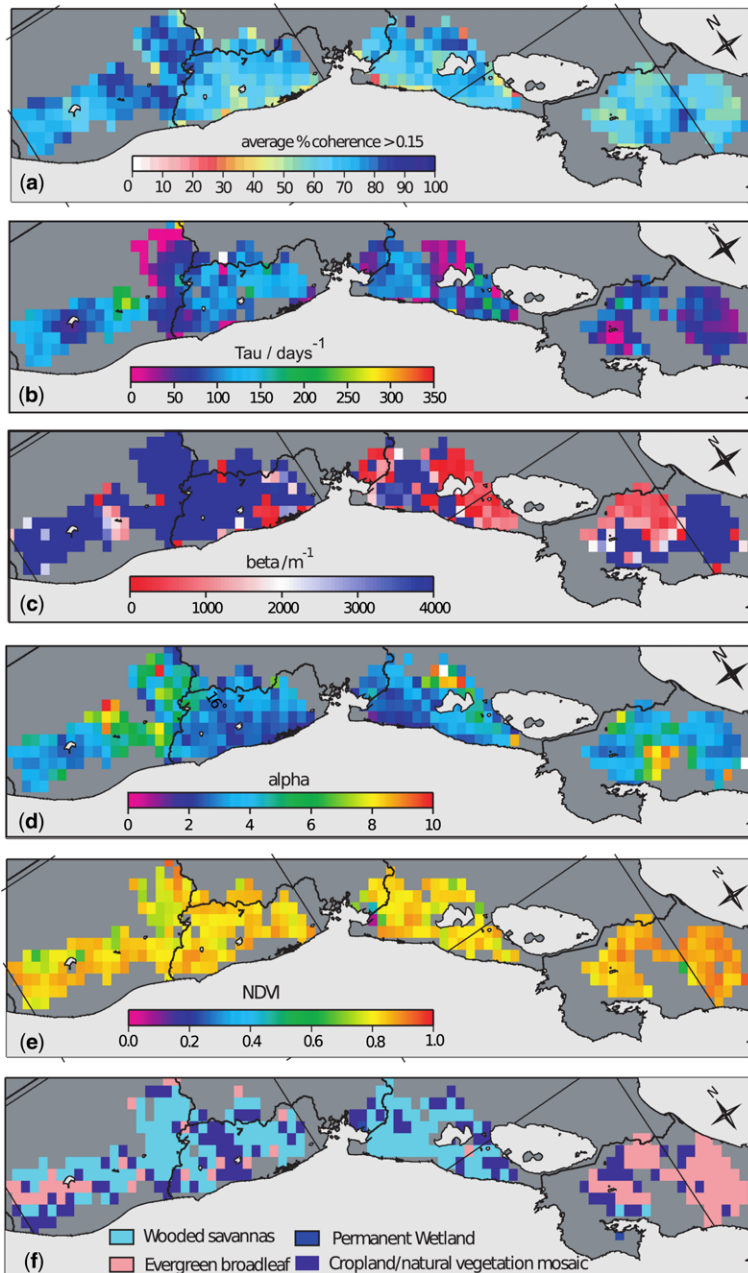


**Fig. 11.** (a) Map of mean percentage of pixels with correlation above 0.15 per box. This figure simply shows the mean values for our input dataset and makes no distinction for temporal or spatial baseline. (b) Map of Central America showing parameter  $\tau$ , describing relative rate of decorrelation as a function of time (lower values indicate faster decorrelation). (c) Parameter  $\beta$ , describing the relative rate of decorrelation as a function of baseline. Where the colour scale is saturated,  $\beta$  values are very high (exceeding 10 000), indicating that coherence is not strongly dependent on baseline. (d) Parameter  $\alpha$  describes the strength of any seasonal dependence of decorrelation (lower values indicate greater seasonal effect). (e) NDVI from MODIS level 3 'atmosphere' product at  $1^\circ$  resolution, resampled to the same resolution as our calculations of  $\tau$ . (f) Land-use map from MODIS level 3 'land' product, resampled to  $0.1^\circ \times 0.1^\circ$  resolution. Land use is classified according to the International Geosphere-Biosphere Programme (IGBP) index.

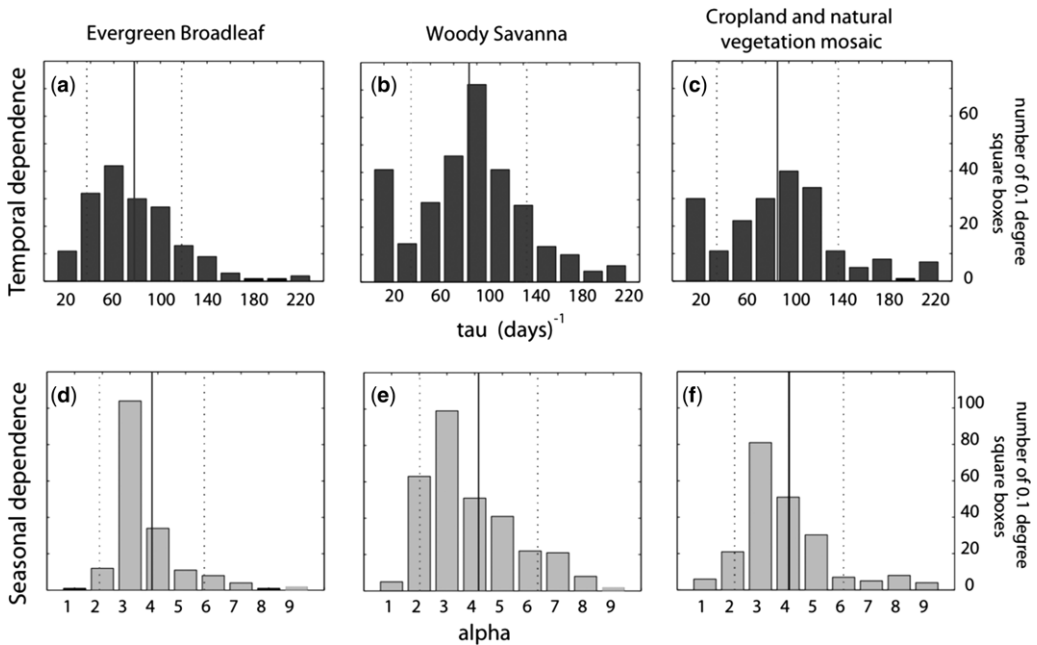


**Fig. 12.** Histograms showing distribution of values for IGBP classifications (a) ‘Evergreen broadleaf’, (b) ‘Woody savanna’ and (c) ‘Cropland/natural vegetation mosaic’ environments. (d), (e) & (f) show distributions of  $\alpha$ . Dotted lines show the mean value.

rates (e.g. Fransson *et al.* 2001; Liu *et al.* 2001). We might, therefore, expect the Normalized Difference Vegetation Index (NDVI) to be a useful predictor for interferometric coherence. Correlations between NDVI and coherence have been observed in data from other parts of the world (e.g. Hawaii: Rosen *et al.* 1996; NW China, Liu *et al.* 2010), with higher NDVI values being associated with poor coherence. In Central America, however, there is no systematic relationship between NDVI and either  $\tau$  or  $\alpha$  (Fig. 12b, d, e). NDVI varies very little across Central America (although it takes slightly higher values in Costa Rica than further north) because vegetation index is similar for both rainforest and cultivated land. Comparison of NDVI with a MODIS land-cover map using International Geosphere–Biosphere Programme (IGBP) classifications shows no clear relationship between type of land cover and NDVI (Fig. 11e, f).

The temporal parameter  $\tau$  and, to some extent, our seasonal parameter  $\alpha$  show distinct distributions for areas of different IGBP land-use classification (Fig. 12). For ‘Evergreen broadleaf,’ dominated by tropical rainforest and cloud forests in Central America,  $\tau$  has a left-skewed distribution with a mode interval of 50–70  $\text{day}^{-1}$  (Fig. 12a). The less densely vegetated land, ‘Cropland/vegetation’ and ‘Woody savanna’, decorrelate less quickly (modes

of 90–110  $\text{day}^{-1}$ : Fig. 12b, c). These classifications are likely to include more developed landscapes, including agricultural areas where surface scatterers are regularly altered due to human activity (e.g. ploughing, harvesting). We attribute the high number of pixels showing very low values for  $\tau$  in these categories to be caused by human interference with the landscape.

Our parameter describing the seasonal dependence of coherence,  $\alpha$ , takes an average value of 2.5 across all land-cover classifications, suggesting some seasonal trends in coherence across the whole area of study (Fig. 12d–f). The distribution in values is slightly more left-skewed in the ‘Evergreen broadleaf’ land-cover category than where vegetation was less dense, a feature we attribute to seasonal agricultural practices increasing the numbers of low values for  $\alpha$ . Seasonal effects are smallest over high topography in Guatemala, Costa Rica and NW of Lake Managua in Nicaragua, and largest in the coastal regions of El Salvador and Nicaragua. We see a very small range of values for  $\alpha$  in areas dominated by rainforest (‘Evergreen broadleaf’: Fig. 12d), and much greater seasonal variation where land-use category suggests some degree of cultivation (Fig. 12e, f).

We use the IGBP land-use classifications to make coarse predictions of decorrelation rate for

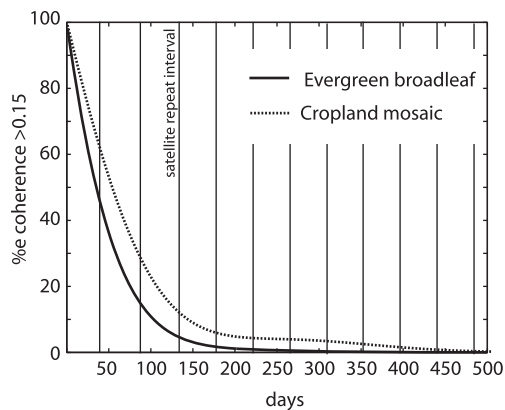


**Fig. 13.** Graph showing predicted decorrelation as a function of time for ‘Evergreen broadleaf’ (mostly rainforest) and ‘Cropland/natural vegetation mosaic’ land uses.

different land types. On average, we expect rainforest environments to decorrelate faster than cropland (Fig. 13), with the largest differences between the two environments in the shortest possible interferograms (46 and 92 days for ALOS). However, this simple approach will not capture the detailed spatial patterns of coherence seen in Figure 11a. The IBGP classifications ‘Cropland/vegetation mosaic’ and ‘Woody savanna’, in particular, deviate from a normal or skewed normal distribution of the temporal decorrelation parameter,  $\tau$  (Fig. 12b, c). There are significant parts of Central America where these environments decorrelate much more quickly than the average, as shown by the peaks at low values for  $\tau$  in Figure 12b, c.

#### *SAR wavelength comparison: Arenal, Costa Rica*

Data from four different satellite instruments (ERS, RadarSat, ALOS and TSX; see Table 2) were used to make measurements at Arenal Volcano, Costa

Rica, which is known to be deforming (Ebmeier *et al.* 2010). To make a meaningful comparison of coherence between these different platforms we use the average value for a section of the interferogram over Lake Arenal as a ‘threshold’ value for interferometric correlation. As reflected and back-scattered radiation from the lake surface will be completely incoherent, any value below this threshold shows that data are unusable. The actual value of this threshold will depend on a combination of the factors listed above (see the ‘InSAR’ and ‘Coherence model’ subsections), but the percentage of pixels above threshold coherence will show the proportion of data that may yield useful interferometric deformation measurements. The percentage of pixels above the given threshold value are shown in Figure 14, and are plotted with respect to temporal and spatial baseline in Figure 15.

Phase correlation in the area around Arenal is among the lowest in Central America, with high phase correlation exclusively over the young lava around the volcano in the majority of interferograms. As expected, owing to its longer wavelength, L-band data produce the greatest proportion of pixels over the coherence threshold, followed by the TSX interferogram, which has a smaller pixel size. All of the TSX interferograms constructed showed significantly better coherence than ERS or RadarSat interferograms of equivalent temporal length. The proportion of pixels above threshold coherence were generally slightly higher in the RadarSat than in the few ERS interferograms, and this is probably due to shorter perpendicular baselines (Fig. 15b).

Although L-band data produce the greatest proportion of coherent pixels, over extremely stable surfaces such as lava flows we find that RadarSat data maintain coherence for up to 600 days (Fig. 15a), illustrating that C-band data are useful for measuring the deformation of small, stable areas. To date, only L-band data have been demonstrated to be suitable for surveying arcs as a whole in the tropics (e.g. Philiposian & Simons 2011). High-resolution, short-repeat-time X-band InSAR data

**Table 2.** SAR satellite instrument parameters referred to in the text

Instrument	Period operational	Wavelength (cm)	Repeat interval (days)	Typical look angle (°)	Range resolution (m)	Azimuth resolution (m)
ERS-1/2 (ESA)	1992–2000/ 1995–2011	5.66 (C-band)	35	c. 23	10	5
ALOS (JAXA)	2006–2011	23.61 (L-band)	46	10–51	9–30	10
RadarSat-1/2 (CSA)	1995/2007–	5.66 (C-band)	24	20–49	25	25
TerraSAR-X (DLR)	2008–	3.12 (X-band)	11	20–45	2–3	3
SENTINEL (ESA)	2013–onwards?	5.66 (C-band)	12	20–46	5	5

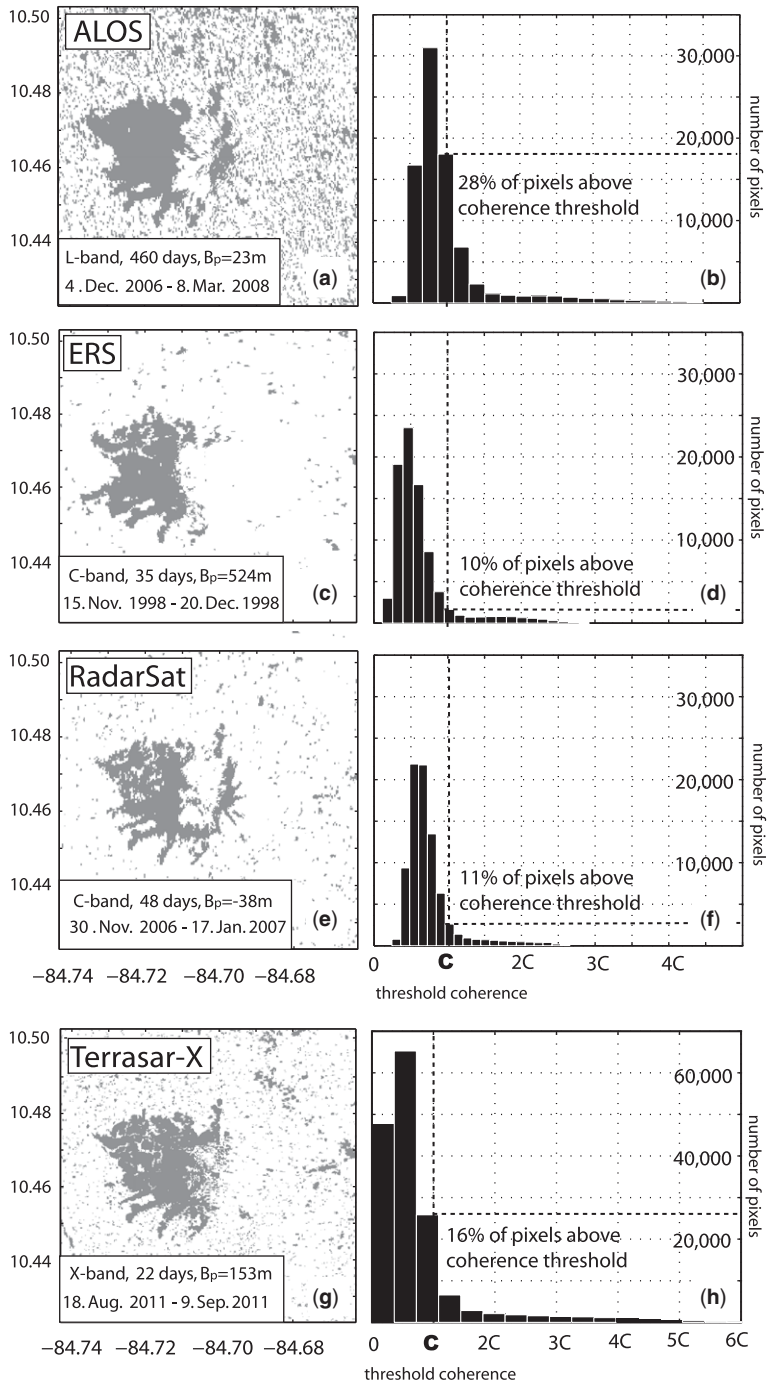


**Fig. 14.** Maps showing pixels above (grey) and below (white) the threshold coherence around Arenal for (a) ALOS, (c) ERS, (e) RadarSat and (g) Terrasar-X interferograms. Threshold values were found from the mean correlation value over part of Lake Arenal and were 0.18, 0.3, 0.35 and 0.1, respectively. Corresponding histograms show the distribution of pixels about this value. The boundary between data above and below the coherence threshold value is marked with a dotted line. Note the different scales on the x- and y-axes for the TSX data. The data points corresponding to each of the interferograms shown here are marked on Figure 15 by black boxes.

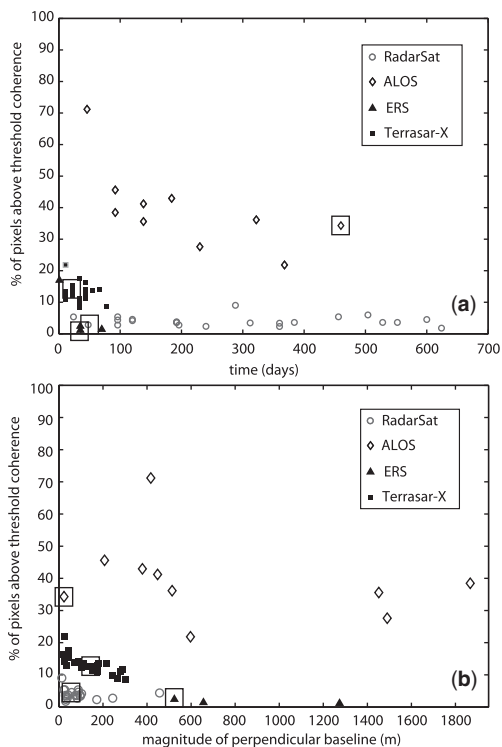


**Fig. 15.** Percentage of pixels above threshold coherence calculated for our complete dataset at Volcàn Arenal, Costa Rica, shown as a function of (a) time span and (b) magnitude of perpendicular baseline. The interferograms shown in Figure 14 are indicated by black boxes.

may prove useful for individual volcanoes but is currently prohibitively expensive for large-scale mapping. The upcoming European Space Agency instrument, Sentinel (Table 2), will be C-band but have a higher spatial resolution and shorter repeat time than ERS and RadarSat. We therefore expect these new data to be much more useful than earlier C-band instruments, although it seems unlikely that it will be as suitable for regional-scale surveys in the way that the ALOS L-band data are. These results agree with expectations (e.g. Rosen *et al.* 1996), but this is the first time that coherence has been quantified for such a large dataset.

## Summary

Our analysis of data from Central America demonstrates factors that determine the usefulness of InSAR at volcanoes both within the tropics and worldwide. In summary, water vapour artefacts and poor coherence are the greatest challenges to making successful InSAR measurements at

volcanoes. This means that the characteristics of volcanoes worldwide that inhibit measurement of deformation with InSAR include: (1) vegetation cover that leaves little of the ground exposed (e.g. rainforest); (2) persistent activity changing surface scatterer properties; (3) steep slopes; and (4) large contrasts in topography. Thus, young stratovolcanoes present particularly difficult targets for measurement with InSAR. Recent activity can, however, present some advantages for InSAR as young lavas present more stable scattering surfaces for InSAR than older, densely vegetated slopes. Steep slopes at many volcanoes also make acquisition and analysis strategy (i.e. including both ascending and descending tracks) more important than in other geographical settings.

Two of the most important limiting factors for measuring volcano deformation with InSAR – water vapour artefacts and vegetation-related loss of coherence – are particularly significant in the tropics. Root mean squared variations in path delay due to stratified water vapour changes reached as much as 6.4, 5.3 and 4.8 cm at Santa Ana, Pacaya and Fuego, respectively (Fig. 6). For our data, this variability in path delay over a volcano is proportional to the difference between edifice height and the surrounding topography (gradient of 2 cm/km height). Although the presence of water vapour artefacts does not prevent InSAR phase measurements from being made, it may mask deformation signals, complicating interpretation at volcanoes with high relief. Furthermore, very steep slopes can lead to layover and foreshortening in the radar geometry (Fig. 8). One satellite look angle is not necessarily sufficient to be sure of detecting deformation.

In Central America, the lower slopes of most volcanoes as well as the surrounding areas are vegetated to some extent. The degree to which this affects InSAR measurement depends on the type and density of vegetation, and has implications for the measurement of deeper magmatic movement. In general, decorrelation rates are greater in the southern arc than in the north, although there is considerable variability (Fig. 11a). Although there is no relationship with NDVI, coherence shows some consistent variation with land-use type, such that decorrelation rates are higher and standard deviation lower for tropical rainforest than for cultivated land (Fig. 12).

Our comparison of L-, C- and X-band results in one of the least coherent parts of Central America demonstrates the importance of having L-band data for measuring volcano deformation in the tropics (Figs 14 & 15). The application of C-band data of varying spatial resolutions is limited to small, stable areas. X-band radar shows potential for penetrating vegetation to allow measurements

over a larger spatial area, but only over short (<100 day) time periods, and where it is possible to obtain a high-resolution DEM. We expect Sentinel data to perform better than ERS or RadarSat data due both to its shorter proposed repeat time and its higher spatial resolution. It is unlikely, however, to allow measurements over regions as large as for L-band data in tropical areas.

All ALOS data were acquired through the WInSAR programme at the University of Miami from JAXA via the Alaskan Satellite Facility. This work was supported by the National Environmental Research Council through the National Centre for Earth Observation (NCEO), of which the Centre for the Observation and Modelling of Earthquakes, Volcanoes and Tectonics (COMET+) is a part. S. K. Ebmeier is supported by an NCEO studentship and J. Biggs was funded by the ESA Changing Earth Science Network and a Rosenstiel Podoctoral Fellowship at the University of Miami. We thank M. Shirzaei and M. Pritchard for their helpful reviews.

## References

- AHMED, R., SIQUEIRA, P., HENSLEY, S., CHAPMAN, B. & BERGEN, K. 2011. A survey of temporal decorrelation from spaceborne L-Band repeat-pass InSAR. *Remote Sensing of Environment*, **115**, 2887–2896, <http://dx.doi.org/10.1016/j.rse.2010.03.017>
- BALZTER, H. 2001. Forest mapping and monitoring with interferometric synthetic aperture radar (InSAR). *Progress in Physical Geography*, **25**, 159–177, <http://dx.doi.org/10.1177/030913330102500201>
- BEAUDUCEL, F., BRIOLE, P. & FROGER, J. 2000. Volcano-wide fringes in ERS synthetic aperture radar interferograms of Etna (1992–1998): deformation or tropospheric effect? *Journal of Geophysical Research*, **105**, 16 391–16 402, <http://dx.doi.org/10.1029/2000JB900095>
- BERARDINO, P., FORNARO, G., LANARI, R. & SANSOSTI, E. 2002. A new algorithm for surface deformation monitoring based on small baseline differential SAR interferograms. *IEEE Transactions on Geoscience and Remote Sensing*, **40**, 2375–2383, <http://dx.doi.org/10.1109/TGRS.2002.803792>
- BEVIS, M., BUSINGER, S., HERRING, T. A., ROCKEN, C., ANTHES, R. A. & WARE, R. H. 1992. GPS meteorology: remote sensing of atmospheric water vapor using the Global Positioning System. *Journal of Geophysical Research*, **97**, 15 787–15 801.
- BIGGS, J., WRIGHT, T., LU, Z. & PARSONS, B. 2007. Multi interferogram method for measuring interseismic deformation: Denali Fault, Alaska. *Geophysical Journal International*, **170**, 1165–1179, <http://dx.doi.org/10.1111/j.1365-246X.2007.03415.x>
- BIGGS, J., ANTHONY, E. Y. & EBINGER, C. J. 2009. Multiple inflation and deflation events at Kenyan volcanoes, East African Rift. *Geology*, **37**, <http://dx.doi.org/10.1130/G30133A.1>
- BIGGS, J., MOTHESE, P., RUIZ, M., AMELUNG, F., DIXON, T. H., BAKER, S. & HONG, S.-H. 2010. Stratovolcano growth by co-eruptive intrusion: the 2008 eruption of Tungurahua Ecuador. *Geophysical Research Letters*, **37**, L21302.
- BÜRGMANN, R., ROSEN, P. A. & FIELDING, E. J. 2000. Synthetic aperture radar interferometry to measure Earth's surface topography and its deformation. *Annual Review of Earth and Planetary Sciences*, **28**, 169–209.
- CARR, M. 1984. Symmetrical and segmented variation of physical and geochemical characteristics of the Central American volcanic front. *Journal of Volcanology and Geothermal Research*, **20**, 231–252, [http://dx.doi.org/10.1016/0377-0273\(84\)90041-6](http://dx.doi.org/10.1016/0377-0273(84)90041-6)
- EBMEIER, S. K., BIGGS, J., MATHER, T. A., WADGE, G. & AMELUNG, F. 2010. Steady downslope movement on the western flank of Arenal volcano, Costa Rica. *Geochemistry, Geophysics, Geosystems*, **11**, Q12004, <http://dx.doi.org/10.1029/2010GC003263>
- EBMEIER, S. K., BIGGS, J., MATHER, T. A., ELLIOTT, J. R., WADGE, G. & AMELUNG, F. 2012. Measuring large topographic change with InSAR: lava thicknesses, extrusion rate and subsidence rate at Santiaguito volcano, Guatemala. *Earth and Planetary Science Letters*, **335–336**, 216–225, <http://dx.doi.org/10.1016/j.epsl.2012.04.027>
- FERRETTI, A., PRATI, C. & ROCCA, F. 2001. Permanent scatterers in SAR interferometry. *IEEE Transactions on Geoscience and Remote Sensing*, **39**, 8–20.
- FOSTER, J., BROOKS, B., CHERUBINI, T., SHACAT, C., BUSINGER, S. & WERNER, C. L. 2006. Mitigating atmospheric noise for InSAR using a high resolution weather model. *Geophysical Research Letters*, **33**, 16 304, <http://dx.doi.org/10.1029/2006GL026781>
- FOURNIER, T. J., FREYMUELLER, J. & CERVELLI, P. 2009. Tracking magma volume recovery at Okmok volcano using GPS and an unscented Kalman filter. *Journal of Geophysical Research*, **114**, B02405, <http://dx.doi.org/10.1029/2008JB005837>
- FOURNIER, T. J., PRITCHARD, M. E. & RIDDICK, S. N. 2010. Duration, magnitude, and frequency of subaerial volcano deformation events: new results from Latin America using InSAR and a global synthesis. *Geochemistry, Geophysics, Geosystems*, **11**, 1003, <http://dx.doi.org/10.1029/2009GC002558>
- FOURNIER, T., PRITCHARD, M. E. & FINNEGAN, N. 2011. Accounting for atmospheric delays in InSAR data in a search for long-wavelength deformation in South America, *IEEE Trans. Geoscience and Remote Sensing*, **99**, 1–12, <http://dx.doi.org/10.1109/TGRS.2011.2139217>
- FRANSSON, J. E. S., SMITH, G. & ASKNE, J. 2001. Stem volume estimation in boreal forests using ERS-1/2 coherence and SPOT XS optical data. *International Journal of Remote Sensing*, **22**, 2777–2791, <http://dx.doi.org/10.1080/01431160010006872>
- GOLDSTEIN, R., ZEBKER, H. & WERNER, C. 1988. Satellite Radar Interferometry: two dimensional phase unwrapping. *Radio Science*, **23**, 713–720.
- HAMLING, I. J., AYELE, A. ET AL. 2009. Geodetic observations of the ongoing Dabbahu rifting episode: new dyke intrusions in 2006 and 2007. *Geophysical Journal International*, **178**, 989–1003, <http://dx.doi.org/10.1111/j.1365-246X.2009.04163.x>
- HANSEN, R. F. 2001. *Radar Interferometry Data Interpretation and Error Analysis*. Kluwer Academic, Dordrecht.

- HELENO, S. I. N., FRISCHKNECHT, C., D'OREYE, N., LIMA, J. N. P., FARIA, B., WALL, R. & KERVYN, F. 2010. Seasonal tropospheric influence on SAR interferograms near the ITCZ – The case of Fogo Volcano and Mount Cameroon. *Journal of African Earth Sciences*, **58**, 833–856, <http://dx.doi.org/10.1016/j.jafrearsci.2009.07.013>
- JOLIVET, R., GRANDIN, R., LASSERRE, C., DOIN, M.-P. & PELTZER, G. 2011. Systematic InSAR tropospheric phase delay corrections from global meteorological reanalysis data. *Geophysical Research Letters*, **38**, L17311, <http://dx.doi.org/10.1029/2011GL048757>
- JÓNSSON, S., ZEBKER, H., SEGALL, P. & AMELUNG, F. 2002. Fault slip distribution of the 1999 M w 7.1 Hector Mine, California, earthquake, estimated from satellite radar and GPS measurements. *Bulletin of the Seismological Society of America*, **92**, 1377–1389.
- LI, Z., MULLER, J., CROSS, P. & FIELDING, E. J. 2005. Interferometric synthetic aperture radar (InSAR) atmospheric correction: GPS, Moderate Resolution Imaging Spectroradiometer (MODIS), and InSAR integration. *Journal of Geophysical Research (Solid Earth)*, **110**, B93410, <http://dx.doi.org/10.1029/2004JB003446>
- LI, Z., MULLER, J.-P., CROSS, P., ALBERT, P., FISCHER, J. & BENNARTZ, R. 2006. Assessment of the potential of MERIS near-infrared water vapour products to correct ASAR interferometric measurements. *International Journal of Remote Sensing*, **27**, 349–365, <http://dx.doi.org/10.1080/01431160500307342>
- LIN, Y.-N., SIMONS, M., HETLAND, E. A., MUSÈ, P. & DiCAPRIO, C. 2010. A multi-scale approach to estimating topographically correlated propagation delays in radar interferometry. *Geochemistry, Geophysics, Geosystems*, **11**, Q09002, <http://dx.doi.org/10.1029/2010GC003228>
- LIU, J. G., BLACK, A., LEE, H., HANAIZUMI, H. & MOORE, J. M. 2001. Land surface change detection in a desert area in Algeria using multi-temporal ERS SAR coherence images. *International Journal of Remote Sensing*, **22**, 2463–2477, <http://dx.doi.org/10.1080/01431160152497673>
- LIU, G., LI, J. *ET AL.* 2010. Surface deformation associated with the 2008 Ms8.0 Wenchuan earthquake from ALOS L-band SAR interferometry. *International Journal of Applied Earth Observation and Geoinformation*, **12**, 496–505.
- LOHMANN, R. B. & SIMONS, M. 2005. Some thoughts on the use of InSAR data to constrain models of surface deformation: noise structure and data downsampling. *Geochemistry, Geophysics, Geosystems*, **6**, Q01007, <http://dx.doi.org/10.1029/2004GC000841>
- LU, Z. & DZURISIN, D. 2010. Ground surface deformation patterns, magma supply, and magma storage at Okmok volcano, Alaska, from InSAR analysis: 2. Coeruptive deformation July–August 2008. *Journal of Geophysical Research (Solid Earth)*, **115**, B00B03, <http://dx.doi.org/10.1029/2009JB006970>
- LUNDGREN, P., USAI, S., SANSOSTI, E., LANARI, R., TESAURO, M., FORNARO, G. & BERARDINO, P. 2001. Modeling surface deformation with synthetic aperture radar interferometry at Campi Flegrei caldera. *Journal of Geophysical Research*, **106**, 19 355–19 367.
- MARTINI, F., TASSI, F., VASELLI, O., DEL POTRO, R., MARTINEZ, M., VAN DEL LAAT, R. & FERNANDEZ, E. 2010. Geophysical, geochemical and geodetical signals of reawakening at Turrialba volcano (Costa Rica) after almost 150 years of quiescence. *Journal of Volcanology and Geothermal Research*, **198**, 416–432, <http://dx.doi.org/10.1016/j.jvolgeores.2010.09.021>
- MASSONNET, D. & FEIGL, K. L. 1995. Discrimination of geophysical phenomena in satellite radar interferograms. *Geophysical Research Letters*, **22**, 1537–1540, <http://dx.doi.org/10.1029/95GL00711>
- MASSONNET, D. & FEIGL, K. L. 1998. Radar interferometry and its application to changes in the Earth's surface. *Reviews of Geophysics*, **36**, 441–500.
- MASSONNET, D., BRIOLE, P. & ARNAUD, A. 1995. Deflation of Mount Etna monitored by spaceborne radar interferometry. *Nature*, **375**, 567–570, <http://dx.doi.org/10.1038/375567a0>
- PARKS, M. M., BIGGS, J., MATHER, T. A., PYLE, D. M., AMELUNG, F., MONSALVE, M. L. & NARVÁEZ MEDINA, L. 2011. Co-eruptive subsidence at Galeras identified during an InSAR survey of Colombian volcanoes (2006–2009). *Journal of Volcanology and Geothermal Research*, **202**, 228–240, <http://dx.doi.org/10.1016/j.jvolgeores.2011.02.007>
- PAVEZ, A., REMY, D. *ET AL.* 2006. Insight into ground deformations at Lascar volcano (Chile) from SAR interferometry, photogrammetry and GPS data: implications on volcano dynamics and future space monitoring. *Remote Sensing of Environment*, **100**, 307–320, <http://dx.doi.org/10.1016/j.rse.2005.10.013>
- PHILIBOSIAN, B. & SIMONS, M. 2011. A survey of volcanic deformation on Java using ALOS PALSAR interferometric time series. *Geochemistry, Geophysics, Geosystems*, **12**, Q11004, <http://dx.doi.org/10.1029/2011GC003775>
- PINEL, V., HOOPER, A., DE LA CRUZ-REYNA, S., REYES-DAVILA, G., DOIN, M. P. & BASCOU, P. 2011. The challenging retrieval of the displacement field from InSAR data for andesitic stratovolcanoes: case study of Popocatepetl and Colima Volcano, Mexico. *Journal of Volcanology and Geothermal Research*, **200**, 49–61, <http://dx.doi.org/10.1016/j.jvolgeores.2010.12.002>
- PRITCHARD, M. E. & SIMONS, M. 2004. An InSAR-based survey of volcanic deformation in the central Andes. *Geochemistry, Geophysics, Geosystems*, **5**, Q02002, <http://dx.doi.org/10.1029/2003GC000610>
- REMY, D., BONVALOT, S., BRIOLE, P. & MURAKAMI, M. 2003. Accurate measurements of tropospheric effects in volcanic areas from SAR interferometry data: application to Sakurajima volcano (Japan). *Earth and Planetary Science Letters*, **213**, 299–310, [http://dx.doi.org/10.1016/S0012-821X\(03\)00331-5](http://dx.doi.org/10.1016/S0012-821X(03)00331-5)
- REUTER, H., NELSON, A., STROBL, P., MEHL, W. & JARVIS, A. 2009. A first assessment of ASTER GDEM tiles for absolute accuracy, relative accuracy and terrain parameters. In: *Geoscience and Remote Sensing Symposium, 2009. IGARSS '09. IEEE International, Volume 5*. Institute of Electrical and Electronics Engineers (IEEE), Piscataway, NJ, 240–243, <http://dx.doi.org/10.1109/IGARSS.2009.5417688>

- RODRIGUEZ, E. & MARTIN, J. M. 1992. Theory and design of interferometric synthetic aperture radars. *IEEE Proceedings: Radar and Signal Processing*, **139**, 147–159.
- RODRIGUEZ, E., MORRIS, C. S. & BEIZ, J. E. 2006. A global assessment of the SRTM performance. *Photogrammetric Engineering and Remote Sensing*, **72**, 249–260.
- ROSEN, P., HENSLEY, S., ZEBKER, H., WEBB, F. & FIELDING, E. 1996. Surface deformation and coherence measurements of Kilauea volcano, Hawaii, from SIR-C radar interferometry. *Journal of Geophysical Research*, **101**, 23 109–23 125.
- ROSEN, P., HENSLEY, S., GURROLA, E., ROGEZ, F., CHAN, S., MARTIN, J. & RODRIGUEZ, E. 2001. SRTM C-band topographic data: quality assessments and calibration activities. In: *Geoscience and Remote Sensing Symposium, 2001. IGARSS '01. IEEE 2001 International, Volume 2*. Institute of Electrical and Electronics Engineers, Piscataway, NJ, 739–741, <http://dx.doi.org/10.1109/IGARSS.2001.976620>
- ROSEN, P. A., HENSLEY, S., PELTZER, G. & SIMONS, M. 2004. Updated repeat orbit interferometry package released. *EOS, Transactions of the American Geophysical Union*, **85**, 47.
- SANTORO, M., ASKNE, J., SMITH, G. & FRANSSON, J. E. S. 2002. Stem volume retrieval in boreal forests from ERS-1/2 interferometry. *Remote Sensing of Environment*, **81**, 19–35, ISSN 0034-4257, [http://dx.doi.org/10.1016/S0034-4257\(01\)00329-7](http://dx.doi.org/10.1016/S0034-4257(01)00329-7)
- SCHMIDT, D. A. & BÜRGMANN, R. 2003. Time-dependent land uplift and subsidence in the Santa Clara valley, California, from a large interferometric synthetic aperture radar data set. *Journal of Geophysical Research*, **108**, 2416, <http://dx.doi.org/10.1029/2002JB002267>
- SEYMOUR, M. & CUMMING, I. 1994. Maximum likelihood estimation for SAR interferometry. In: *Geoscience and Remote Sensing Symposium, 1994. IGARSS '94. Surface and Atmospheric Remote Sensing: Technologies, Data Analysis and Interpretation. IEEE International, Volume 4*. Institute of Electrical and Electronics Engineers, Piscataway, NJ, 2272–2275, <http://dx.doi.org/10.1109/IGARSS.1994.399711>
- SHIRZAEI, M. & BÜRGMANN, R. 2012. Topography correlated atmospheric delay correction in radar interferometry using wavelet transforms. *Geophysical Research Letters*, **39**, L01305, <http://dx.doi.org/10.1029/2011GL049971>
- STEVENS, N. F. & WADGE, G. 2004. Towards operational repeat-pass SAR interferometry at active volcanoes. *Natural Hazards*, **33**, 47–76, <http://dx.doi.org/10.1023/B:NHAZ.0000035005.45346.2b>
- STEVENS, N. F., WADGE, G., WILLIAMS, C. A., MORLEY, J. G., MULLER, J., MURRAY, J. B. & UPTON, M. 2001. Surface movements of emplaced lava flows measured by synthetic aperture radar interferometry. *Journal of Geophysical Research*, **106**, 11 293–11 314, <http://dx.doi.org/10.1029/2000JB900425>
- WADGE, G., WEBLEY, P. W. ET AL. 2002. Atmospheric models, GPS and InSAR measurements of the tropospheric water vapour field over Mount Etna. *Geophysical Research Letters*, **29**, 190, <http://dx.doi.org/10.1029/2002GL015159>
- WADGE, G., MATTIOLI, G. S. & HERD, R. A. 2006. Ground deformation at Soufriere Hills Volcano, Montserrat during 1998–2000 measured by radar interferometry and GPS. *Journal of Volcanology and Geothermal Research*, **152**, 157–173, <http://dx.doi.org/10.1016/j.jvolgeores.2005.11.007>
- WADGE, G., ZHU, M., HOLLEY, R. J., JAMES, I. N., CLARK, P. A., WANG, C. & WOODAGE, M. J. 2010. Correction of atmospheric delay effects in radar interferometry using a nested mesoscale atmospheric model. *Journal of Applied Geophysics*, **72**, 141–149.
- WEBLEY, P., WADGE, G. & JAMES, I. N. 2004. Determining radio wave delay by nonhydrostatic atmospheric modelling of water vapour over mountains. *Physics and Chemistry of the Earth*, **29**, 139–148, <http://dx.doi.org/10.1016/j.pce.2004.01.013>
- WICKS, C. W., DZURISIN, D., INGEBRITSEN, S., THATCHER, W., LU, Z. & IVERSON, J. 2002. Magmatic activity beneath the quiescent Three Sisters volcanic center, central Oregon Cascade Range, USA. *Geophysical Research Letters*, **29**, 070, <http://dx.doi.org/10.1029/2001GL014205>
- ZEBKER, H. A. & VILLASENOR, J. 1992. Decorrelation in interferometric radar echoes. *IEEE Transactions on Geoscience and Remote Sensing*, **30**, 950–959, <http://dx.doi.org/10.1109/36.175330>
- ZEBKER, H. A., ROSEN, P. A. & HENSLEY, S. 1997. Atmospheric effects in interferometric synthetic aperture radar surface deformation and topographic maps. *Journal of Geophysical Research*, **102**, 7547–7564, <http://dx.doi.org/10.1029/96JB03804>
- ZEBKER, H., AMELUNG, F. & JONSSON, S. 2000. Remote sensing of volcano surface and internal processing using radar interferometry. In: MOUGINIS-MARK, P., CRISP, J. & FINK, J. (eds) *Remote Sensing of Active Volcanism*. American Geophysical Union, Geophysical Monograph, **116**, 179–205.